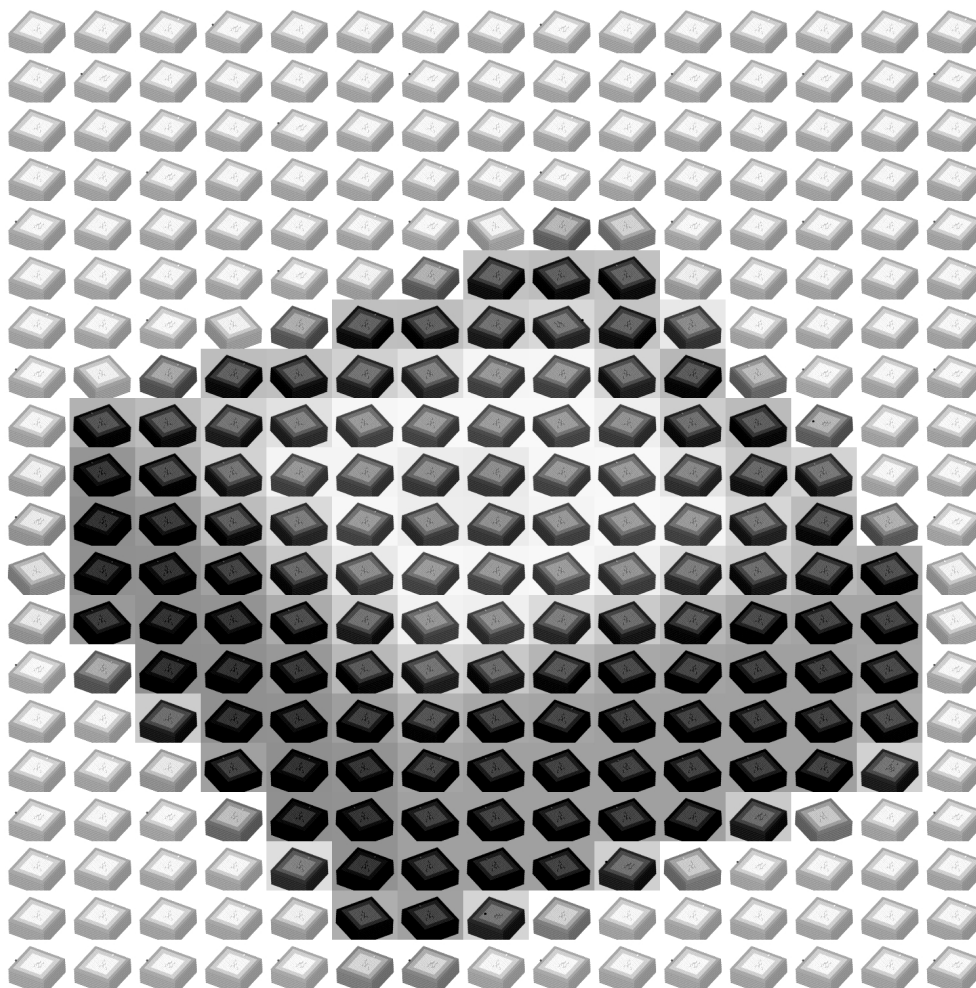


Ar^+ 's impact on $Cu(001)$

A combined study of Molecular Dynamics and Kinetic Monte-Carlo simulations and Scanning Tunneling
Microscopy experiments of sputtering processes on $Cu(001)$.

Master thesis



by

Tjeerd Bollmann

August 2006

Exam committee:

Prof.Dr.ir. B. Poelsema

Dr.ir. H. Wormeester

Dr.ir. W.K. den Otter

Dr. R. van Gastel

ir. F.L.W. Rabbering

ir. F.G. Stoian

University of Twente

Solid State Physics

P.O. Box 217

7500 AE Enschede

The Netherlands

Shoot for the moon. Even if you miss it, you'll land among the stars.

Less Brown

Abstract

To be able to simulate the evolution of the surface morphology of $Cu(001)$ after Ar -ion bombardment we perform Molecular Dynamics and experiments to model a single ion impact.

In this thesis we used Molecular Dynamics simulations to find the sputtering-, adatom-, interstitials- and surface- and bulk vacancies after the impact of an Ar -ion on the $Cu(001)$ surface. Combining this with a random impact position we found a sputtering yield of about 3-4 atoms for temperatures up to 150K, for higher temperatures the sputtering yield increases. The adatom yield is found to be 2-8 atoms and the vacancy yield is found to be 4-8 monovacancies. In our simulations we hardly find evidence for the creation of bulk vacancies on impact. Interstitials are created but almost immediately anneal to the surface.

In order to analyse single ion impacts using the Scanning Tunneling Microscope we perform experiments using a low ion dose and low temperature. For low fluence we find that one single Ar -ion impact on $Cu(001)$ creates on average one vacancy cluster of about 6-7 monovacancies and 1-2 adatom cluster of about 7 atoms each. We determined the sputtering yield from experiments at high temperatures and higher ion doses. These experiments result in a sputtering yield of about 0.2 atoms per ion.

Using a Kinetic Monte-Carlo algorithm we are able to calculate the evolution of the surface morphology using very simple models for the Ar -ion impact on $Cu(001)$. We compare qualitatively the results with those obtained from performed experiments.

Contents

Preface	I
1 Review	1
1.1 Introduction	1
1.2 (Pre)history of erosion simulation	1
1.3 Conclusion	3
1.4 Is sputtering inverse homoepitaxial deposition?	3
1.5 Conclusion and new approach	4
2 Molecular Dynamics simulations	6
2.1 Introduction	6
2.2 Simulation Method	6
2.3 Results	13
2.4 Discussion	18
2.5 Conclusions	19
3 Kinetic Monte-Carlo simulations	20
3.1 Introduction	20
3.2 Simulation Method	20
3.3 Simple sputter model	22
3.4 Advanced sputter model	22
3.5 Conclusion	23
4 Experimental results	27
4.1 Introduction	27
4.2 Experimental	27
4.3 Single ion impacts	30
4.4 Temperature dependence	31
4.5 Conclusion	31
5 Conclusions	34
References and Notes	36
Appendix A	38

Preface

In this thesis we present the results of a combined study of Molecular Dynamics and Kinetic Monte-Carlo simulations and Scanning Tunneling Microscopy of sputtering processes on $Cu(001)$. Before we start to obtain results we will review the most important simulations done so far and discuss the difference between the "world" of adatoms and vacancies in chapter 1. We will also discuss our new approach in general.

In chapter 2 we discuss the Molecular-Dynamics simulation algorithm developed for this project. We discuss briefly the algorithm techniques and other tricks used to get a better feeling for the limitations of the model. We proceed by presenting the results for the energy and temperature dependence of the Ar -ion impact on $Cu(001)$. In this chapter we also discuss the improvements that can be made to get even more reliable results. To get a feeling for the evolution of the surface morphology after a low dose of ion bombardment we use two simple sputtering models in a Kinetic Monte-Carlo algorithm in chapter 3. Here our theoretical exercises end.

In chapter 4 we present the results of the performed experiments using the Scanning Tunneling Microscope. We discuss the three major problems for determining accurate sputtering yields.

We end this thesis with chapter 5 where we discuss the comparison between the simulations and experiments performed. We also make some recommendations and suggestions for future research work.

At that point my journey in the world of Ar atoms hitting Cu atoms ended (for now). I have been dealing with diffusions and impacts on $Cu(001)$ for almost 10 months and I still get more and more fascinated about all the processes that play a fundamental role. At this point it is time to say thanks to a lot of people. Without their help this work would not be able.

At first I want to thank Prof. Bene Poelsema for the opportunity to write my master-thesis in his group. I also want to thank Dr. Herbert Wormeester for this interesting subject. I want to say thanks to my daily supervisor for the simulation part ir. Frits Rabbering and for the experimental part ir. Georgiana Stoian for endless enthusiasm and commitment. I also want to thank both of you for your their endless patience, especially when I asked you to answer one of my thousand "why?"-questions. I also want to thank Dr. ir. Wouter den Otter for willing to be the external committee member and help me out with some MD problems, Dr. Raoul van Gastel for the enjoying discussions and all members of the VSF group who made my graduation period a nice time to remember.

My deepest gratitude goes to my parents. Thanks for believing in me, for supporting me, for loving me, and for being there. Above all, and as always, my special thanks to my dear, patient, incomparable girlfriend Sherien. A big kiss for her.

Enschede, August 25, 2006

Tjeerd Bollmann

Chapter 1

Review

1.1 Introduction

Thin film technology has become an important technology in the fabrication of many modern devices such as large scale integrated circuits and optical thin films. To improve the performance of thin films and to miniaturize the dimensions of electronic circuits (for e.g. information storage) the use of controlled patterning is very interesting. A versatile technique also used for nanopatterning is the sputter-erosion technique. The method is based on the removal of atoms on the surface by the impact of ions. The key parameters in this process are the deposition rate and the incident ion energy. The incident angle is also an important [1] parameter. In miniaturizing the dimensions a qualitative and quantitative good understanding of this process (and in special the sputtering process) is needed. A lot of experimental work is done on this subject using e.g. AFM and STM methods. Although these methods have atomic resolution they have observational difficulties (think e.g. about the difficulties to measure monovacancies) at the very small scale and can therefore not fully unveil the mysteries in these morphologies. The sputtering process is therefore difficult to understand fully from experiments. A way to get more information is by using simulation techniques. Two commonly used simulation techniques are Molecular-Dynamics (MD) [2] and Kinetic Monte-Carlo (KMC) [3].

1.2 (Pre)history of erosion simulation

On many surfaces, patterning of the surface results in stripe patterns. These patterns are usually explained by the mechanisms introduced by Bradley and Harper [4]. Although this theory is still quite successful, it has the disadvantage of a continuum model in that it gives only a coarse-grained description of the process. It completely neglects the atomic diffusion processes that are fundamental for the full comprehension of this phenomenon.

In this chapter we will describe two simple but important approaches that were used in the past to describe the temporal evolution of morphologies created by ion erosion. The first one was done by Teichert in 1992 [5] describing an $Ag(100)$ -surface after sputtering with 600eV Ar^+ -ions. The second one was done by Hartmann in 2002 [6]. Although the idea of using Sigmund's sputtering theory [7] is more used they combined it with a KMC simulation.

1.2.1 Teichert's approach

From his LEED-patterns on sputtered $Ag(100)$ surfaces, Teichert concludes that after ion bombardment the atoms will return on their ideal lattice position quite fast. Therefore a Solid-On-Solid (SOS) model in which only surface atoms are allowed to be removed, can be used. No overhangs nor bulk vacancies are allowed, which is quite realistic since they will annihilate at the surface for longer timescales. The surface is described as a

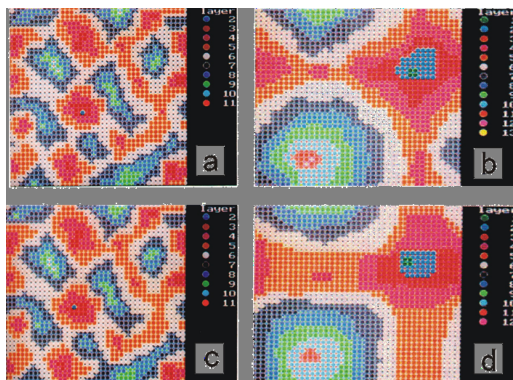


Fig. 1.1: Simulation results for sputtering for 6MLE @ 170K (a) and 300K (b). After annealing for 2 minutes @ 170K (c) and 0.3 seconds @ 300K (d). Taken from [5].

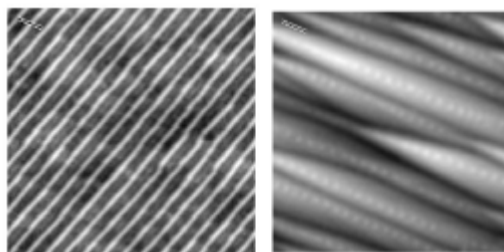


Fig. 1.2: Surfaces after long time sputtering at an angle of incidence of 50° with Wolf-Villain (a) and activated surface diffusion (b) type surface diffusion. Taken from [6].

2-dimensional field of discrete height variables on an fcc(100) lattice with periodic boundary conditions. In this model the damage created by a single impact is equal to one (randomly picked) surface atom removed. For the diffusion only moves to the nearest-neighbour (NN) fourfold hollow (4FH) site are taken into account. The activation energy for both the intra- and interlayer diffusion processes are calculated using a Morse potential. For a complete list of diffusion barriers see [5] page 35-38.

A simulation done by Teichert of the sputtering of a Ag(100) surface at both 170K and 300K showed that during the sputtering there is no qualitative difference (see figure 1.1). Although the structures at 300K are larger the geometry is the same. For low temperature (170K) there is hardly any difference in the morphology during and shortly after sputtering, the ratio of $\langle 100 \rangle$ and $\langle 110 \rangle$ -facets is 1.07 immediately after sputtering and 1.08 after annealing. For higher temperature (300K) this ratio increases from 1.16 to 2.04, which can also be clearly seen from figure 1.1.

1.2.2 Hartman's approach

Hartman uses the same SOS-model as Teichert did, albeit for a simple square lattice. Now two processes take place: relaxation and erosion. For an erosion step a random position above the surface is chosen and the ion penetrates a distance under the surface (with a certain incidence angle). There it stops and distributes its energy. Now the energy which the surface atoms obtains is calculated using Sigmund's theory. The particle on the surface is removed with a probability proportional to the energy. For the surface relaxation two diffusion schemes are used: activated surface diffusion and Wolf-Villain as simplified models of high-temperature and low-temperature schemes. As can be seen from figure 1.2 the long time behaviour is not qualitative equal.

1.3 Conclusion

Although the model used by Teichert is for Ag(100), the results for sputtering on Cu(001) at normal incidence at 200K and 330K look remarkably similar [1]. Ion flux and temperature play an important role. The main difference between Ag(100) and Cu(001) however is the absence of an Ehrlich-Schwöbel barrier for Ag (although it is low for Cu). The impact model of Teichert's approach is too simple: there are e.g. no adatoms created (compare with [8]). We also expect more damage for an 800eV impact. Off-normal sputtering is also impossible using this simple model.

The model of Hartman does include grazing incidence. It is however based upon a simple square lattice, although the most interesting metals (e.g. Ni, Pd, Pt, Cu, Ag, Au, Al) are fcc crystals. Hartman also used the most simple types of relaxation and since they give different results for long timescale we should be careful to draw any conclusions from that. Although the impact process is a little bit more advanced, it's still too simple to be realistic.

1.4 Is sputtering inverse homoepitaxial deposition?

Assuming the sputtering event as equivalent to a "negative deposition" where adatoms are replaced by surface vacancies has often been the input for computational models [8]. This model looks from an experimental point of view too simple and from the random walks of adatom clusters and vacancy clusters can also be concluded that adatoms behave different from vacancies and we might therefore not expect ion sputtering as "negative deposition". To underline this statement we compared the diffusivity for clusters up to three atoms on a Cu(001) surface. The thermal motion of an atom/vacancy on an ideal lattice results in a random walk (since we have equal distances and a random direction). From this random walk we can determine the ratio of the mean-square displacement $\langle r^2 \rangle$ to time τ which is known as the diffusion coefficient or diffusivity D [9] which is equal to the hopping frequency using an energy barrier E_{diff} :

$$D = \frac{1}{z} \frac{\sum \langle r^2 \rangle}{\tau} = \nu_0 \exp(-E_{diff}/k_B T) \quad (1.1)$$

where z is two times the number of dimensions since it equals the number of neighbouring sites and ν_0 the attempt frequency ($\nu_0 = 1 \times 10^{13} s^{-1}$). The adatom diffusion coefficient of the center of mass for adatom clusters up to three atoms for three different temperatures is already known from literature [10]. The values found by our KMC simulation (for more details on the KMC code see chapter 3, for the EAM hopping energy barriers [11]) are in agreement with these values (see table 1.4).

Since the single adatom is stable it has an infinite lifetime. We have to note that the adatom dimer is stable since the bond breaking energy for the NN configuration is $E_8 = 0.811 eV$ and for the next-nearest-neighbour (NNN) is $E_2 - E_4 + E_1 = 0.843 eV$ (see figure 1.3). These high values guarantee the dimer stability. The dimer diffusion is a two step process involving a move with barrier $E_2 = 0.463 eV$ followed by a move with $E_4 = 0.183 eV$. The first step is the rate limiting one and since $E_2 \approx E_0$ the diffusion coefficients are of the same order (see table 1.4). The dimer lifetime can be calculated using equation 1.1 and is e.g. 57 minutes @ 263K. The adatom trimer has a very low diffusivity which is caused by the variety of paths. Their lifetime is even higher than for a dimer (the breaking energy is e.g. $E_3 - E_4 + E_1 = 0.920 eV$ see figure 1.3).

The vacancies behave however different from adatoms. The monovacancy is stable but has a huge diffusivity compared to the single adatom. This is caused by its low hopping energy barrier $E_{127} = 0.280 eV$, which is in (qualitative) agreement with indirect STM experiments on a single vacancy using an indium/copper surface alloy where a diffusion barrier of $0.232 eV$ is obtained [12]. The divacancy will preferentially make a random walk in one dimension since $E_{63} = 0.530$ (see figure 1.3). This is also a two step process with barrier E_{127} followed by E_{119} in which the first step is the rate limiting one. The "cheapest" way to break up is using two times E_{127} . This costs only $E_{127} + E_{127} - E_{119} = 0.430 eV$ while staying "alive" costs $E_{127} + E_{130} = 0.410 eV$. Therefore a divacancy is not stable and has a lifetime of only $3 \times 10^{-5} s$ @ 263K. The trimer can split into a monovacancy and a divacancy and therefore has the same lifetime.

We can conclude that small vacancy clusters will immediately break up into monovacancies which are very mobile. Small adatom clusters are however very stable (in the order of hours). The high diffusivity of mono-

vacancies suggests that surface vacancies will be rapidly absorbed at the step edges or at vacancy clusters of at least four vacancies. These large vacancy-islands are expected to influence the morphological development of the growing surface. The interested reader is referred to a theoretical study of diffusion and stability of small vacancy clusters on Cu(100) using TAD [13] which is in qualitative agreement with our conclusions. Therefore we can conclude that sputtering is not equal to "negative deposition" and has to be modeled more advanced to give agreement with experimental results.

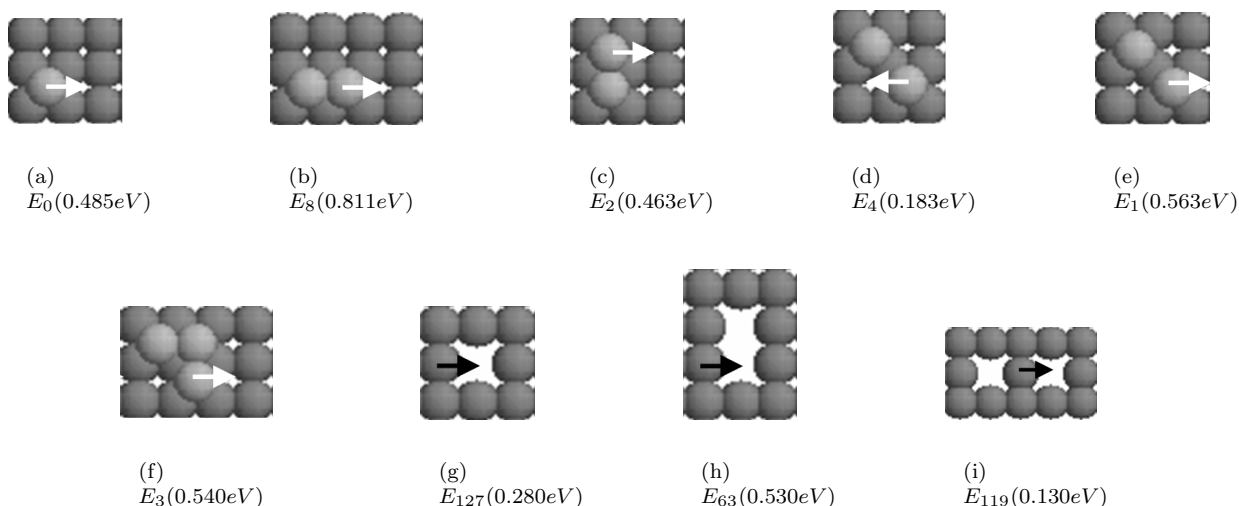


Fig. 1.3: Important hopping energy barriers for diffusions and breakups of small adatom and vacancy clusters [11].

$T(K)$	D_1^{ad} (sites/s)	D_2^{ad} (sites/s)	D_3^{ad} (sites/s)
213	3.36 ± 0.17	5.77 ± 0.23	0.079 ± 0.001
223	11.0 ± 0.5	17.7 ± 1.0	0.292 ± 0.002
263	507 ± 24	706 ± 36	19.4 ± 0.3

Table 1.1: Diffusion coefficients calculated from simulations for the adatom (D_1^{ad}), -dimer (D_2^{ad}) and the -trimer (D_3^{ad}) for three temperatures. This is in agreement with [10] table II.

$T(K)$	D_1^{vac} (sites/s)	D_2^{vac} (sites/s)	D_3^{vac} (sites/s)
213	$(4.7 \pm 0.1) \times 10^5$	$(1.08 \pm 0.01) \times 10^5$	0.0922 ± 0.0006
223	$(2.4 \pm 0.1) \times 10^5$	$(2.61 \pm 0.01) \times 10^5$	0.356 ± 0.001
263	$(4.3 \pm 0.1) \times 10^6$	$(2.21 \pm 0.01) \times 10^6$	26.0 ± 0.1

Table 1.2: Diffusion coefficients calculated from simulations for the monovacancy (D_1^{vac}), dimer- (D_2^{vac}) and the trimer- (D_3^{vac}) for three temperatures.

1.5 Conclusion and new approach

In conclusion we can say that the approaches so far have not been realistic enough to be comparable to experimental work. The sputtering process can not be described by just a inverse deposition. Therefore we will try

a different approach which is more detailed and takes the best from both MD and KMC. Since the energy of a single ion impact will spread out fast, we only need a calculation for a few ps which can be covered by MD. All diffusion processes have at room temperature typically activation energies in the order of a few tenth of an eV . These processes will therefore occur on a timescale of μs which can be covered by KMC. So to extend the time scale we can couple an MD to a KMC code. This combination can be described as follows:

- A MD simulation is started for a crystal at a certain temperature during an ion impact. Dependent on the incident energy of the ion it will take some time before all collisional processes are over and the crystal has reached the target temperature which is within 10 degrees from the initial one. For low energies a few ps will be enough.
- At the end of the MD simulation the energy is minimized and we categorize the different defects. After doing statistics on this we create a model which accurately describes an "average" impact.
- Now a KMC simulation is started using this model.

Thus the coupling of the MD simulation to a KMC simulation allows us to extend our calculations from a few ps up to seconds before the next particle will hit the surface, which is quite realistic for a typical sputtering experiment.

Molecular Dynamics simulations

2.1 Introduction

Computer experiments play a very important role in today's scientific research. Since computer power has increased there has been a new region between experiment and theory: the computer experiment or simulation. When computer power increased the complexity of these experiments has increased thereby opening a new road to a better understanding of experiments. Simulations therefore bring theoretical models "to life" and can often come very close to real experiments: the computer experiments can sometimes be compared directly to experimental results. When this happens, with simulations we have a powerful tool to understand and interpret experiments at the microscopic level and study regions which are not experimentally accessible.

A Molecular Dynamics (MD) simulation is a technique to compute the movement of a set of atoms over time by integrating their equations of motion. MD is all about the laws of classical dynamics, in special Newton's second law: $\mathbf{F} = m\mathbf{a}$. Using MD we can get a better understanding of the processes that play an important role in an energetic particle-solid collision of Ar^+ on $Cu(001)$.

In this chapter we discuss the results of our MD simulations of an energetic particle-solid collision. To simulate this we used a somewhat modified MD code which prevents us from the nonphysical reflection of energy from the boundaries in our model. We will briefly discuss the MD code (which can be found on [14]) we used and the modifications we applied before we present the results.

2.2 Simulation Method

Potential

The main ingredient for every simulation is a model of the physical system we are investigating. In a MD simulation this comes down to choosing a potential. In our MD we use the (common) Lennard-Jones 12-6 (LJ) potential for the $Cu(001)$ substrate and Ar -ion. The LJ potential and force are given by the expression:

$$V_{LJ}(r) = 4\epsilon \left[\left(\frac{\sigma}{r} \right)^{12} - \left(\frac{\sigma}{r} \right)^6 \right] \quad (2.1)$$

$$F_{LJ}(r) = -\nabla_r V_{LJ}(r) \quad (2.2)$$

for an interaction between two atoms. The potential consists of two parts: an attractive tail dominated by the term $\sim 1/r^6$ and a strongly repulsive part at shorter distances dominated by the term $\sim 1/r^{12}$. The exponent 12 is chosen on a practical basis: the potential is very easy to compute. The potential has a minimum around 1.122σ and the well has a depth equal to ϵ . In table 2.1 we summarized the values for ϵ and σ for Cu and Ar . From the mixing rules of Lorentz and Berthelot [15] we can approximate the values for $Ar - Cu$. In figure 2.1 we plotted the potentials using these values.

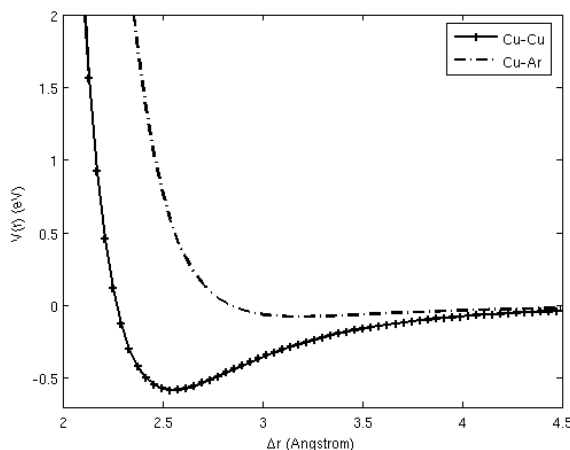


Fig. 2.1: LJ-potentials for $Cu - Cu$ and $Cu - Ar$. The $Cu - Ar$ potential is almost purely repulsive.

	σ	ϵ
Cu-Cu	2.33	0.5828
Ar-Ar	3.41	0.0103
Cu-Ar	2.84	0.0776

Table 2.1: The LJ-parameters for Cu and Ar [15].

The potential has an infinite range and therefore every particle would interact with every other particle in the universe. Since the number of interacting particles separated by a distance r increases with r^2 , it would take years (in fact even ages) to compute all these interactions. We therefore define a cutoff radius r_c and we disregard interactions between the atoms that are separated more than r_c . If we would simply truncate the potential like this, particle pairs that cross r_c would induce a (little) jump in the energy. Therefore the potential is shifted to vanish to zero at r_c :

$$V(r) = \begin{cases} V_{LJ}(r) - V_{LJ}(r_c) & \text{if } r \leq r_c \\ 0 & \text{if } r > r_c \end{cases} \quad (2.3)$$

Of course, the potential energy of the model using the truncated and shifted potential slightly differs from the models with untruncated potentials, but we can correct for this. In our MD simulations we use a truncation at 2.5σ which is equal to $\approx 6\text{\AA}$ (which is up to the NNN). Using this cutoff we can calibrate the value for ϵ to the energy for a bulk atom (12 NN and 10 NNN) which is about $7eV$. Choosing a r_c that is larger (3.2σ is also commonly used) increases calculation time and does not effect the results since $V(r_c) = 0.0022eV$.

Substrate layout

In order to model the impact at a constant temperature, the substrate consists of an impact zone (were the ion will hit) embedded in a thermostat which is embedded in a static zone (see figure 2.2) like a Russian doll. The atoms in the impact zone and the thermostat move according to the second law of Newton. The velocities of the atoms in the thermostat zone are modified by a temperature control scheme (see 2.2). The static layer on the outside prevents translations of the system in space. The thermostat zone acts not only as a heat bath but also as a cushion or sandbag to absorb reflected energy waves.

The dimension of the impact zone varies in size depending on the impinging energy. The thermostat zone consists of a wall that is 3 atoms thick. The static layer is 2σ thick which corresponds to r_c .

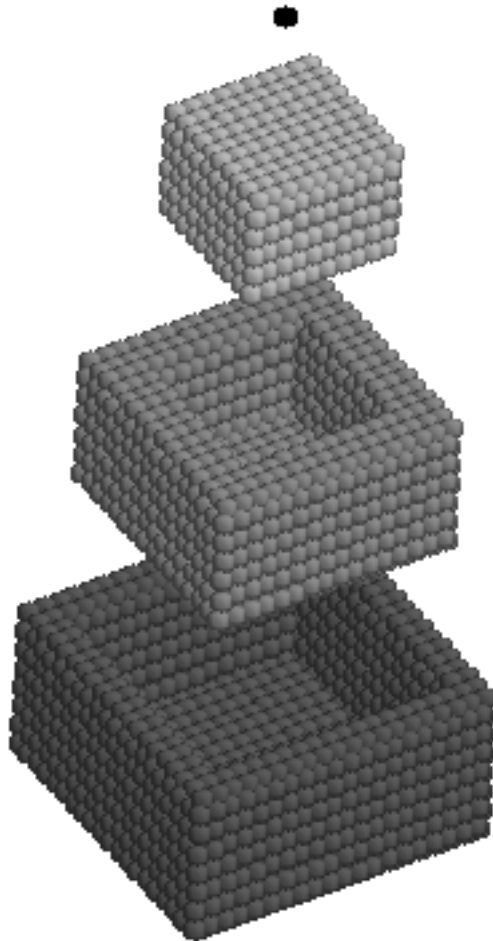


Fig. 2.2: Substrate layout. From top to bottom: the ion, impact zone, thermostat zone, static layer.

Time integration algorithm

The time integration algorithm is the heart of the MD program. It integrates the equation of motion and follows the particles trajectory. Since time is discretized and we want the truncation errors (since we use 64-bit precision in Fortran we do not need to worry about round-off errors) to be as small as possible in each iteration we make use of the popular Verlet algorithm which has a truncation error proportional to δt^4 . The idea of this algorithm is to write two third-order Taylor expansions for the positions. We take one forward and one backward in time where \mathbf{v} is the first derivative, \mathbf{a} the second and \mathbf{b} the third to time:

$$\mathbf{r}(t + \delta t) = \mathbf{r}(t) + \mathbf{v}(t)\delta t + \frac{1}{2}\mathbf{a}(t)\delta t^2 + \frac{1}{6}\mathbf{b}(t)\delta t^3 + O(\delta t^4) \quad (2.4)$$

$$\mathbf{r}(t - \delta t) = \mathbf{r}(t) - \mathbf{v}(t)\delta t + \frac{1}{2}\mathbf{a}(t)\delta t^2 - \frac{1}{6}\mathbf{b}(t)\delta t^3 + O(\delta t^4) \quad (2.5)$$

Now if we add these two equations we see that the truncation error of this algorithm is of the order of δt^4 :

$$\mathbf{r}(t + \delta t) = 2\mathbf{r}(t) - \mathbf{r}(t - \delta t) + \mathbf{a}(t)\delta t^2 + O(\delta t^4) \quad (2.6)$$

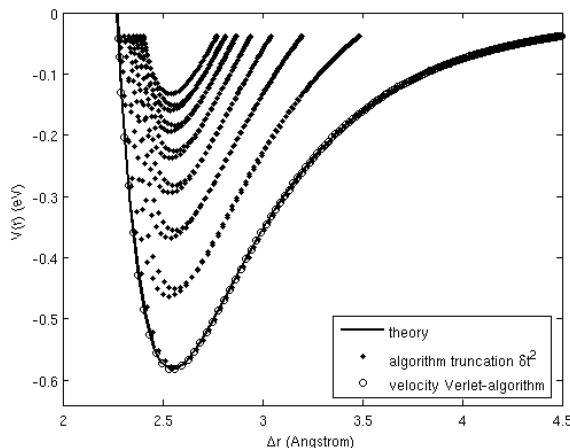


Fig. 2.3: For this figure we let a dynamic *Cu* atom approach a static one. It "bounces" (attraction and repulsion) in the potential well. We plot the theoretical potential for *Cu*–*Cu* and the potential measured using integration with a truncation error of the order of δt^2 compared to the velocity Verlet scheme where the error is of the order of δt^4 .

In this standard Verlet algorithm the velocity is not directly generated and has therefore an error of the order δt^2 . To overcome this problem we use in our MD simulation the velocity Verlet scheme:

$$\mathbf{r}(t + \delta t) = \mathbf{r}(t) + \mathbf{v}(t)\delta t + \frac{1}{2}\mathbf{a}(t)\delta t^2 \quad (2.7)$$

$$\mathbf{v}(t + \frac{1}{2}\delta t) = \mathbf{v}(t) + \frac{1}{2}\mathbf{a}(t)\delta t \quad (2.8)$$

$$\mathbf{a}(t + \delta t) = \frac{\mathbf{F}}{m} \quad (2.9)$$

$$\mathbf{v}(t + \delta t) = \mathbf{v}(t + \frac{1}{2}\delta t) + \frac{1}{2}\mathbf{a}(t + \delta t)\delta t \quad (2.10)$$

In figure 2.3 we illustrate the difference between a integration method in which we have a truncation error of δt and one in which this error is of δt^4 . The graph shows the atom "bouncing" in a potential well. If we have a large truncation error we loose a lot of energy; the well gets less and less deep. This is not in agreement with total energy conservation where the sum E of kinetic K and potential V energy stays constant over time.

Initialization

When starting a simulation we should assign an initial position and velocity to every particle. The initial positions of the Cu-substrate are chosen on a face centered cubic lattice with a lattice constant $a = 3.615\text{\AA}$. Choosing the positions at ideal lattice positions agrees with a temperature of $0K$. To get the desired temperature we draw a velocity from a Maxwell distribution at temperature T . This is done by first drawing velocities from a gaussian distribution in the interval of $[-0.5, 0.5]$ followed by a shift of all velocities such that the total momentum is zero (to prevent translational motion of the whole system) and scaling the resulting velocity to adjust the mean kinetic energy to the desired temperature. Now starting the simulation with these initial positions and velocities will not result in the desired temperature. At $t = t_0$ the system has $V = 0$ and $K = \frac{3}{2}k_B T$. Since the LJ-potential can be approximated by a harmonic oscillator in its minimum and K is also quadratic in velocity half of the kinetic energy will be taken by the potential energy. Therefore the temperature will drop (approximately) to half of the starting temperature. We therefore start the simulation by drawing velocities from a Maxwell distribution at $2T$ (see also figure 2.4).

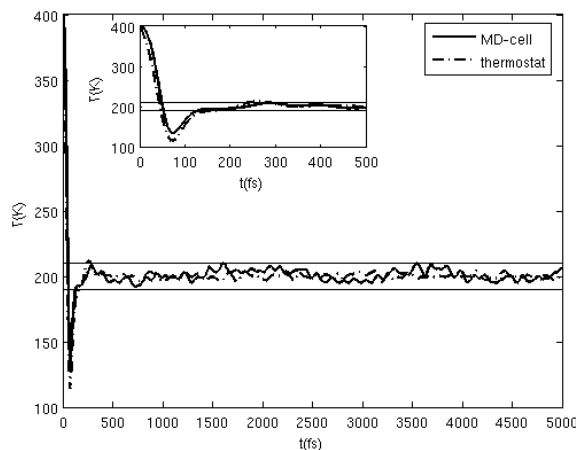


Fig. 2.4: The temporal evolution of the temperature for the MD-cell of $15 \times 15 \times 10$ atoms and a thermostat layer of 3 atoms thick at 200K. The Maxwell distribution is drawn for 400K. The temperature fluctuates for $t > 300fs$ between 190K and 210K.

Energy minimization

Directly after impact we will have a peak in the temperature. This kinetic energy will be conducted away by the thermostat (see also next section). After some time the temperature will be equal (or within 10 degrees) of the initial temperature and the system will be in equilibrium. Then we minimize the energy of the system as if we froze it. The temperature will drop to $\approx 0K$ and we can start our analysis of the defects. The basic idea of energy minimization is to gradually reduce the kinetic energy. The method annihilates the velocities whenever the scalar product of the velocity and force becomes negative. In this way we decrease the temperature drastically until we eventually end up with a very low temperature where the total energy of the system is minimized.

MD at constant temperature

During the collision of the *Ar*-ion on the *Cu*-substrate, the temperature of the substrate will experience a thermal spike. The heat will then be conducted away from the site of the collision quickly into the substrate. To model this we perform a constant temperature MD simulation. The atoms at the boundaries (the static layers) are held fixed to maintain the structure of the substrate. These boundaries can however result in the nonphysical effect of reflection of the energy on the boundary. This reflection could result in artifacts. Therefore we use a method that allows some atoms to absorb the extra energy that is pumped into the system by the ion and that will also successfully control the temperature of the system.

Temperature is a thermodynamic quantity and can be related to the kinetic energy through the principle of equipartition of energy. Therefore we can say that

$$\frac{1}{2}m \langle v^2 \rangle = \frac{Nk_B T}{2} \quad (2.11)$$

where N is the number of degrees of freedom (in our simulation 3 times the number of particles), k_B is the Boltzmann constant and T the thermodynamic temperature. To control the temperature, the velocities of the particles have to be adjusted. One very simple way to do this is to directly scale the velocity of each particle using the equation:

$$\frac{\mathbf{v}_{new}}{\mathbf{v}_{old}} = \sqrt{\frac{T}{T_{system}}} \quad (2.12)$$

This method is called the velocity rescaling method. It adds (or subtracts) energy to (or from) the system

efficiently but brutally stresses the lattice and produces artifacts on the edges. It is therefore far from how the energy is actually dissipated. We therefore choose for the Berendsen method.

Before we introduce this method, it is worthwhile to mention the Andersen method. This method can be thought of as a system that is coupled to a thermal bath that is held at the desired temperature. The coupling is simulated by a random 'collision' of a particle of the system with a thermal particle. After each collision, the velocity of a randomly chosen particle is set to a value randomly drawn from the Maxwell distribution corresponding to the desired temperature (see also before). This method is simple and consistent with the canonical ensemble, but it introduces drastic changes to the dynamics of the system. A relatively gentle approach is the Berentzen method [16], which is perfectly suited for particle-collision simulations [17].

As in the Anderson method, the system is coupled to an imaginary heat bath held at the desired temperature. The exchange of thermal energy is however much more gradual. Instead of a drastic change in the velocity of a particle, the velocity is scaled gradually by multiplying it with a constant:

$$\lambda = \sqrt{1 + \frac{\delta t}{\tau} \left(\frac{T_0}{T} - 1 \right)} \quad (2.13)$$

Here δt is the timestep and τ is the time constant of the coupling. Using the Berendsen method the velocities of the particles are adjusted so that the instantaneous temperature T_0 approaches the desired temperature T . If a strong (weak) coupling is desired, τ will be chosen small (large). A weaker coupling reduces the disturbance of the system. In evaluating their own method [16], Berendsen *et al.* concluded that the static average properties were not significantly affected by the coupling time constant, but the dynamic properties were. They showed that reliable dynamic properties can be derived if the ratio $\delta t/\tau$ is equal to or above 0.01. The Berendsen method has however one serious problem; it does not rigorously reproduce the canonical distribution. In our model we set the ratio $\delta t/\tau$ equal to 0.01 since this gives us the best compromise between an ideal temperature control ($T \pm 10$ degrees without any reflection of energy on the boundaries) and the disturbance of the physical behaviour of the system (e.g. atoms in the thermostat layer that pop out).

Looking at the atoms

The simplest way to probe our system is to "look at it". We display all atoms as balls with a certain radius. Using different colours we represent the different types of atoms in our system. This way we construct in 3D a kind of "photograph" or in (3+1)D a "movie". To visualize these atomic structures we use Rasmol (<http://openrasmol.org/>). It is easy to use and powerful software which is free for both Windows and Linux computers.

Statistical quantities to measure

During the calculation we are interested in some quantities. The most important one is energy conservation: $E = K + V$ where E is the total energy, which should stay constant over time and K and V respectively the kinetic and potential energy. From the kinetic energy we can calculate the instantaneous temperature. Since we use a thermostat too absorb the incoming energy we are also interested in the amount of energy that is absorbed by this layer. We therefore calculate the energy difference before and after the Berendsen method was applied for every timestep. By taking the cumulative sum we end up with the total energy that is absorbed.

Impact properties

For perpendicular incidence the incoming energy can be converted to a velocity using the relation:

$$v_z = \sqrt{2K/m} \quad (2.14)$$

where K is the incident energy and m is the mass of the Argon ion (39.9amu). The ion will hit at random positions on the surface. To make a random position for the impact of the ion we draw two random numbers (x,y). Since Fortran creates pseudorandom numbers we use the sum of the current hours, minutes and seconds to initialize the seed. For perpendicular incidence, symmetry arguments restrict the impact area of interest to

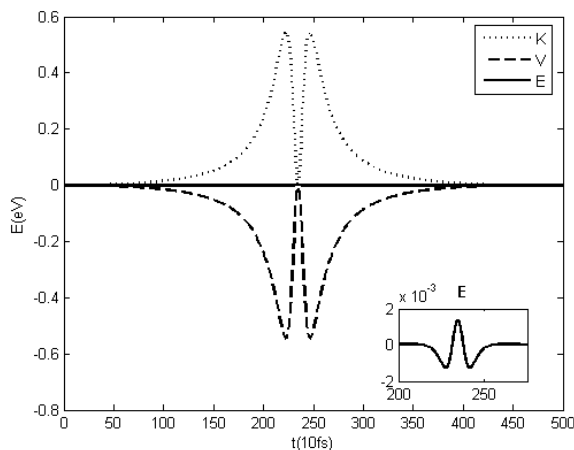


Fig. 2.5: The total E , kinetic K and potential V energy for a "bounce" in the potential well. Notice that due to the velocity Verlet-algorithm energy conservation is not guaranteed for short time, see subfigure (the interested reader is referred to [18] p.62). For long time however it does.

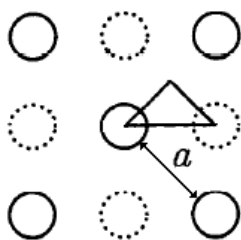


Fig. 2.6: Schematic view on top of the $Cu(001)$ surface. The first layer is drawn solid, the second one dotted. The impact area of interest is due to the symmetry only $1/8$ of the area of the surface primitive cell. The atom in the middle of this figure corresponds to the atom in the middle of the surface of our simulation crystal. a is the lattice constant.

a triangle with an area of only $1/8$ of the area of the surface primitive cell (see also figure 2.6). To be sure to get all random positions from $[0, a/2\sqrt{2}]$ in this cell we use the relation:

$$(x, y) = \begin{cases} (x, y) & \text{if } y \leq x \\ (y, x) & \text{if } y > x \end{cases} \quad (2.15)$$

Saving CPU time

In our model the force calculation is with $\approx 80\%$ of CPU-time the most time consuming operation. By using pairwise interactions (as in almost any MD) we have to evaluate for a system of N particles, $N(N-1)/2$ interactions. Therefore this calculation scales as N^2 if we use no tricks. We therefore included in our algorithm the Verlet-list or neighbour-list (see also figure 2.7). In this method we use a cutoff radius r_v which is slightly larger than r_c to make a neighbour-list of pairs that have a potential interaction. Only those particles within r_c really interact. But if the maximum displacement of the particles is less than $r_v - r_c$ we can calculate the interaction again using the same neighbour-list. The calculation is of the order N . When the sum of the two largest displacements is more than $r_v - r_c$ we have to update the neighbour-list. This operation is of the order

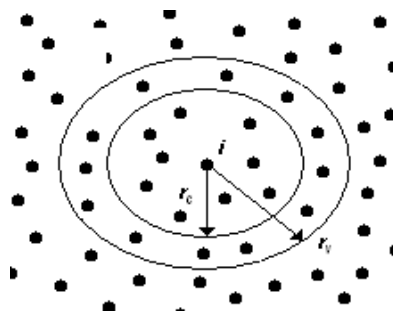


Fig. 2.7: An illustration of the cutoff distances r_c for potential truncation and r_v for neighbour list. The particle i interacts with those particles within r_c , the neighbour list contains all particles within r_v .

N^2 , but since we use the neighbour-list we speed up the evaluation. Theoretically, the computing time could be reduced to the order $N^{3/2}$ depending on the maximum displacement of the particles.

Programming language

For our modelling we use the Fortran language for numeric computation. The language has a long tradition in computational physics and is born in the end of the 50s and became really popular in the 60s and 70s. Fortran is easy to program and is designed for high performance. It is directly compiled (using the Intel[®]-compiler) into machine language and can be compiled for both Windows and Linux. It is easy to reuse parts of code that have been made before and therefore we could follow some MD recipes[18, 19, 15].

2.3 Results

2.3.1 Categorising defects

To be able to use our results from MD simulations in the KMC model we need to categorize all defects. Since we have conservation of mass, the number of atoms that have been displaced by the incoming ion have to be compensated by vacancies. Therefore we have the relation

$$Y_{sp} + Y_{ad} + Y_{in} = Y_{bv} + Y_{sv} \quad (2.16)$$

with Y_{sp} the sputtered yield (in atoms), Y_{ad} the adatom yield, Y_{in} the yield for interstitials, Y_{bv} and Y_{sv} the yield of bulk- and surface vacancies. At high enough temperatures (in the order of 100K), energy barriers can be overcome to anneal the bulk vacancies and interstitials. Some through recombination but most at the surface. Surface vacancies can also be filled by adatoms.

To analyse our results we need a method to categorize these defects. We use the following method (see also figure 2.8):

- If a Cu-atom has moved more than $2r_c$ we call it sputtered.
- If the height of an atom is between $a/2$ and $a/4$ above the initial surface, we call it an adatom (for Cu $a = 3.615$).
- We draw spheres with a radius of $a/(2\sqrt{2})$ around the ideal lattice points and monitor the number of atoms that are found in this sphere. If no atom is found we call it a vacancy.
- If this vacancy has an atom above it we call it a bulk vacancy, otherwise we found a surface vacancy.
- If we found two atoms in this sphere, we call it an interstitial that corresponds to the "dumbbell" configuration.

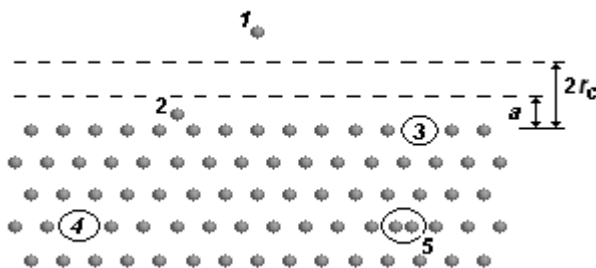


Fig. 2.8: Categorising of defects. Atom 1 is sputtered, 2 is an adatom, 3 a surface vacancy, 4 a bulk vacancy and 5 an interstitial.

In this way all defects are uniquely categorised. We have to note that this method will only work for analysing vacancies in an fcc-lattice. When the impact results in a locally amorphous crystal, we can no longer speak of vacancies. Using relation 2.16 we can always check if all defects are categorized.

2.3.2 Energy dependence

From an experimental point of view we expect for low kinetic energies of the Ar -ion only a small disturbance of the lattice which will not result in any damage. At a certain amount of energy we have overcome the barrier for creating damage and it will be possible to create vacancies and adatoms. The first step to check if our model is in agreement with experiment is to measure at what incidence energy we start to create defects on the surface. To be able to compare all the impacts we let the ion hit at normal incidence at the center of the 4FH site. This implies that we create a "head-on-head" collision in the second layer. The MD-cell is $15 \times 15 \times 10$ atoms in size, the thermostat layer is 3 atoms thick surrounded by a 2 atoms thick static layer. The timestep is $1fs$. To rule out any temperature dependence result we perform these simulations at 1K.

In figure 2.9 we present some snapshots of a $800eV$ impact in the center of the 4FH site (for snapshots of Ar -ion energies $100eV$, $200eV$ and $400eV$ we refer to 5, for animations see [14]). Shortly after the impact the lattice is distorted and the crystal is locally amorph (figure 2.9(a) and 2.9(b)) due to the enormous amount of energy that heats up the substrate locally. Some atoms get kicked out (figure 2.9(c)) and some of these get sputtered (figure 2.9(d)). After that the substrate cools down and the energy is irradiated in a spherical way and gets absorbed by the thermostat. The crystal gets back in its fcc crystal structure and the adatoms lose their kinetic energy and take their final position (figure 2.9(e) and 2.9(f)). The simulation is stopped after $5ps$ and the energy is minimized using the energy minimization method described in 2.2. Now we analyse the substrate and categorise the defects. For figure 2.9(f) we find a $Y_{sp} = 2$, $Y_{ad} = 4$ and a $Y_{sv} = 6$. No bulk vacancies or interstitials were found at $5ps$.

We performed the same simulations using different incidence energies. The results of these simulations are summarized in table 2.2. For very low energies (up to $40eV$) the surface is only "tickled". For higher energies the surfaces gets disturbed but there is no damage created. Starting from (about) $200eV$ we create permanent defects.

After the impact the temperature drops exponentially (see figure 2.10). The Ar -ion leaves the impact with an energy of about $100eV$. In the subfigure of figure 2.10 we calculate the cumulative sum of the absorbed energy for all timesteps. This gives us the total amount of absorbed energy (for this simulation it was $604eV$, for very low energies almost all the energy is absorbed except for the energy of the leaving Ar -ion). To create an adatom we need to break 8 NN-bonds and we create 4 NN-bonds in the new 4FH site. Therefore creation of an adatom has an energy of about $4 \times 0.6eV \approx 2.5eV$. The energy of a sputtered atom is therefore twice this energy. For this simulation the substrate contains after $5ps$ still about $60eV$ of kinetic energy. This can be seen in figure 2.10 as a temperature 10 degrees above the initial temperature.

In summary we can say that the energy dependence of the defect formation is as expected. An impact at the center of the 4FH site results in the formation of permanent defects for energies higher than a $200eV$. We

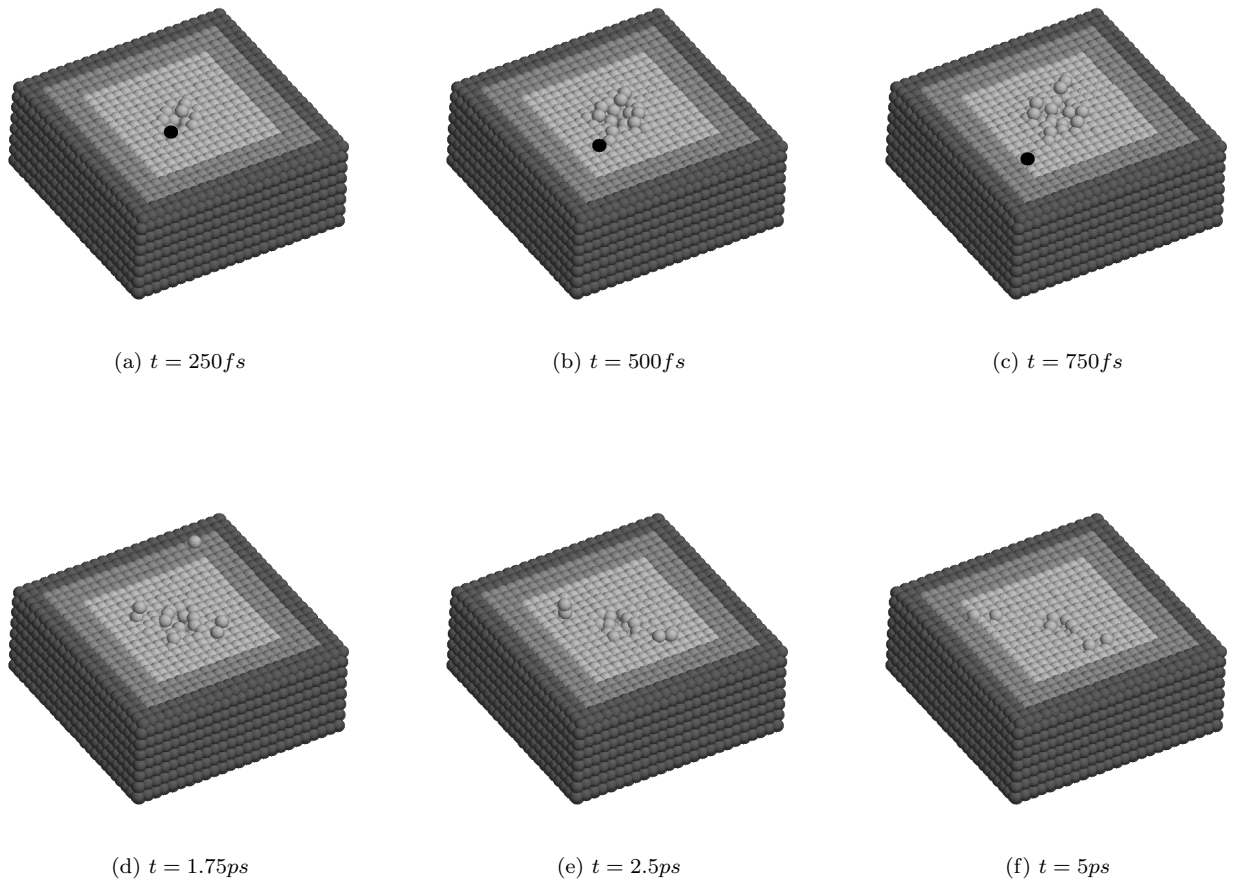


Fig. 2.9: Snapshots (3D) of a $800 eV$ Ar -ion normal incidence impact on the $Cu(001)$ substrate at 1K. See also figure 2.2.

Incidence Energy (eV)	Y_{sp}	Y_{ad}	Y_{in}	Y_{sv}	Y_{bv}
20	0	0	0	0	0
40	0	0	0	0	0
80	0	0	0	0	0
100	0	0	0	0	0
200	0	1	0	1	0
400	3	1	0	4	0
800	2	4	0	6	0

Table 2.2: Energy dependence of crystal defects. All results are at 1K for "head-on-head" collisions.

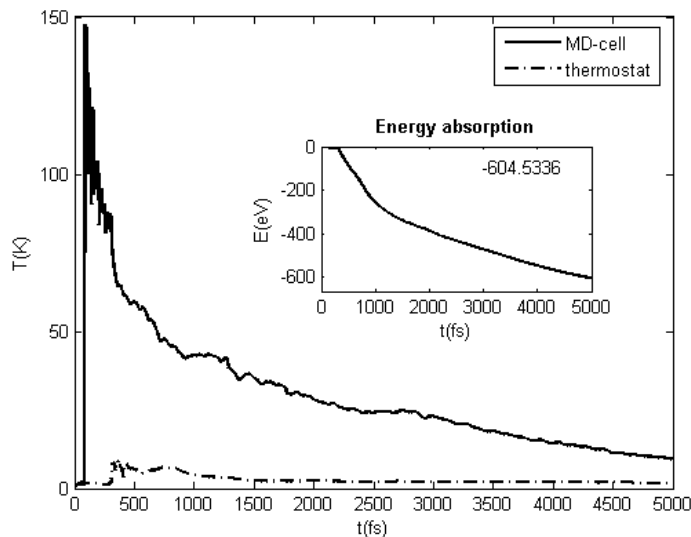


Fig. 2.10: Temporal evolution of the MD-cell and thermostat temperature after a 800eV Ar -ion impact on the $\text{Cu}(001)$ substrate. In the subfigure we calculated the energy absorbed by the thermostat.

have to note that a "head-on-head" collision will rarely occur in experiments.

2.3.3 Temperature dependence

Most MD simulations of impacts are done at very low temperature e.g. 0 or 1K [20, 21]. This is justified by the small thermal motion at the timescale of the impact. A temperature of say 100K is also negligible compared to the locally sometimes 1000K due to the impact. Therefore the approximation of a crystal with atoms at the ideal lattice points (0K) is made. This 100K background temperature can however enable some diffusion processes that are not enabled at 0K. Therefore we expect at least some temperature dependence which we also found in experiments (see chapter 4). To be able to compare to experiments (see chapter 4) we measure the temperature dependence of a 800eV Ar -ion impact on $\text{Cu}(001)$. We initialize the substrate at a certain temperature for 5ps . After that we take a random point for the impact (see also 2.2). For statistics we average all yields over 10 simulations. For the temperatures up to 100K we simulate for 5ps while for 150K and 200K we simulate for 10ps because of the thermal motions that cause the substrate to take longer to reach equilibrium.

In figure 2.11 we present some snapshots for one of the simulations at 150K (for snapshots at 1K, 50K, 100K and 200K we refer to 5, for animations see [14]). As can be clearly seen from these snapshots is that right after the impact we create adatoms and vacancies (figure 2.11(a) and 2.11(b)). At the point of impact the high temperature spike creates a amorph crystal. At this temperature this locally amorph structure seems to be stable. This can also be seen from the radial distribution in figure 2.12.

In table 2.3 we present the results for five different temperatures. We have to note that at higher temperatures we have locally amorph structures that are stable. From these configurations it is not possible to determine the number of surface- and bulkvacancies. Due to our method (see section 2.3.1) we get unrealistic high numbers for the adatom, surface- and bulkvacancy yield for amorph structures. These numbers do not represent real adatoms and vacancies. The sputtering yield stays almost constant for increasing temperature, since the sputtering yield is not influenced by these locally amorph structures.

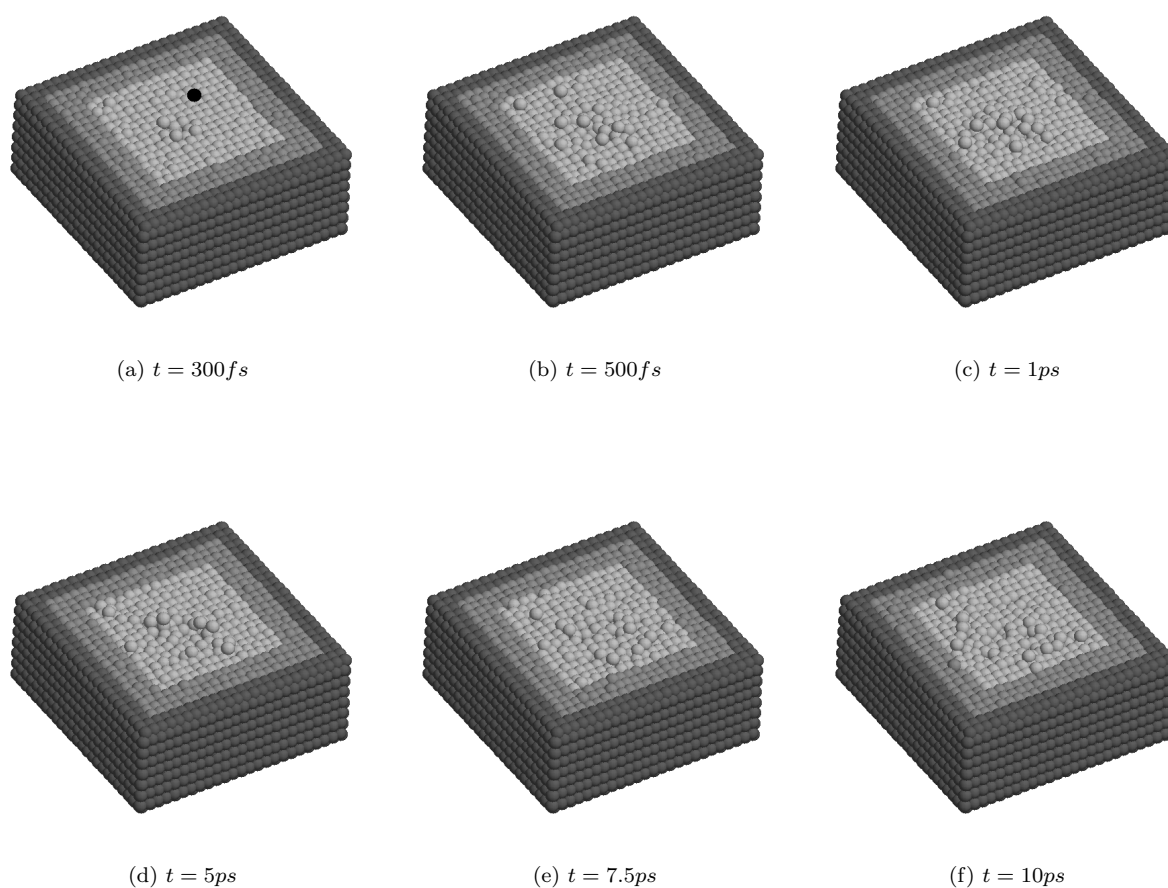


Fig. 2.11: Snapshots (3D) of a $800eV$ Ar -ion normal incidence impact on the $Cu(001)$ substrate at $150K$. See also figure 2.2.

Temperature (K)	Y_{sp}	Y_{ad}	Y_{in}	Y_{sv}	Y_{bv}
1	3.1	1.9	0	4.4	0.6
50	3.8	1.5	0	4.8	0.5
100	4.2	5.1	0	8.3	1.0
150	2.9	7.7	0	44.1	4.2
200	7.5	167.2	1.2	149.7	41.9

Table 2.3: Temperature dependence of crystal defects. All numbers are averaged over 10 simulations with random impact coordinates of $800eV$ Ar^+ at normal incidence on $Cu(001)$. The number in parentheses is .

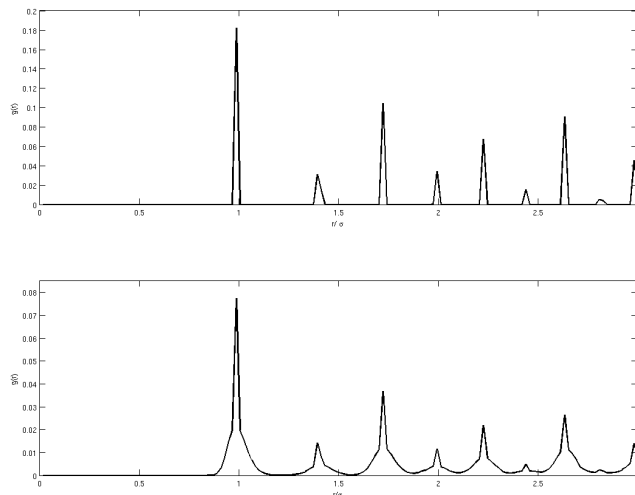


Fig. 2.12: Radial distribution function before impact (upper) and after impact (lower). The atoms clearly pack around each other in 'shells'. Due to impact these peaks get broad. At short distance the radial distribution function is zero indicating the effective width of the atoms: 1σ .

2.4 Discussion

In our MD simulations we make use of a LJ-potential, which is a typical pairwise potential and probably the most used one in MD. In practice however only a limited number of materials in specific cases can be modeled realistic using this potential. In special, metals like *Cu* show a lot of many-body effects. In table 2.4 we summarize three of these effects for some metals.

$E_c/k_B T_m$ is the ratio between the cohesive energy and the melting temperature. For metals this ratio is about 30. For the LJ-potential this ratio is about 3 times lower. This means that metals have some extra cohesion compared to the LJ-potential. Or the other way around, when fitting the LJ-potential to the cohesive energy, it will give a much lower melting point for metals than is realistic. The melting temperature for *Cu* in specific is 1358K. The melting temperature for the system using the LJ-potential is not known. It can be roughly estimated by increasing the temperature of the crystal until diffusion appears.

E_v/E_c is the ratio between the energy needed to create a vacancy and the cohesive energy. This number is somewhere between 0.25 and 0.33 for metals, while it is about 1 for the LJ-potential. If relaxations are neglected it is exactly 1 since in a pairwise potential these two energies are the same as they are both associated with the breaking of 8 *NN*-bonds. In metals this however not the case!

Therefore it would be better to use a more realistic potential which has both a correct cohesive energy and melting temperature as well as a correct vacancy formation energy. A potential that includes these effects is the Embedded Atom Method (EAM). In the EAM method the total energy of an atom is given by the relation:

$$V_{EAM} = \frac{1}{2} \sum_{j \neq i} V(r_{ij}) + F(\bar{\rho}_i) \quad (2.17)$$

Here $V(r_{ij})$ is a pair potential as a function of the distance between atoms i and j like in the LJ-potential. $F(\bar{\rho}_i)$ is the embedding energy as a function of the host electron density $\bar{\rho}_i$ induced at atom i by all the other atoms in the system. This electron density is given by:

$$\bar{\rho}_i = \sum_{j \neq i} \rho(r_{ij}) \quad (2.18)$$

Property	<i>Cu</i>	<i>Ag</i>	<i>Pt</i>	<i>Au</i>	<i>LJ</i>
T_m (K)	1358	1235	2041	1337	not known
$E_c/k_B T_m$	30	28	33	33	13
E_v/E_c	0.33	0.36	0.26	0.25	~ 1

Table 2.4: The melting temperature (T_m) and the ratios of cohesive energy and melting temperature ($E_c/k_B T_m$) and vacancy formation and cohesive energy (E_v/E_c) for some metals and a typical LJ-potential.

where $\rho(r_{ij})$ is the electron density function. Although equation 2.17 is based on certain physical ideas on the bonding in metals, the functions $V(r_{ij})$, $\rho(r_{ij})$ and $F(\bar{\rho}_i)$ have practically lost their meaning and are just used as some fitting functions.

There are good EAM fitting parameters for *Cu*, *Ag*, *Au*, *Ni*, *Pd* and *Pt* available [22]. There is also an improved EAM potential for *Cu* available [23] which gives lattice properties in agreement with experiments (see table III in [23]). Although the possibility of using a potential that is stored in a table (using table look-up followed by linear interpolation) for the *Cu*(001) substrate is included in our algorithm we did not use it for our simulations because of the complications it gives in the algorithm combined with the restricted time for this project. This enables us however to simulate all kinds of particle-solid collision with different materials. We should also combine this potential with another potential for the *Ar* – *Cu* interaction. A very simple approach could be a purely repulsive Molière potential [24]. Using an EAM-potential could give more reliable results since the vacancy formation energy using the LJ-potential is too high and the melting temperature too low which could result in a unphysical large amount of vacancies, which in turn could lead to an overestimated sputtering yield. A higher (and more realistic) melting temperature will also enable us to simulate systems at higher temperatures using the method discussed in 2.2.

The other improvement in the potential is to use an interaction at the long-distance. This is called a long-distance potential. In our model an atom that has moved more than r_c higher than the surface, has no longer any interaction and will continue its uniform motion according to Newton’s first law. This might not be realistic since we expect sputtered atoms with a very low kinetic energy (which is typically about $6eV$ for a $800eV$ *Ar*-ion impact) to be able to be re-attracted to the surface and create adatoms. Therefore the number of sputtered atoms might be overestimated and the number of adatoms underestimated. Their sum however stays constant, no matter if a long-distance potential is used or not.

We could also improve the algorithm by using a timestep that is dependent on the maximum velocity. Using this it will no longer be possible to choose a timestep that is too large (we violate energy conservation) or too small (the simulation will take unnecessary long).

Using this model it is also possible to simulate an off-normal particle-solid collision. We should however keep in mind that for grazing incidence we need a larger substrate which can be at best a rectangle.

2.5 Conclusions

Although the potentials could be improved to model *Cu* more physical realistic, the model used in our MD algorithm gives qualitative good results for an energetic particle-solid collision. Permanent damage to the *Cu*(001) substrate is created for normal incidence *Ar*-ion energies of $200eV$ and higher. The sputtering yield for $800eV$ at normal incidence stays almost constant over temperature. For higher temperatures we see locally stable amorph crystals. For these temperatures we get unrealistic high numbers for the adatom yield and vacancy yield due to the method for categorising defects.

Kinetic Monte-Carlo simulations

3.1 Introduction

In chapter 2 we described the single impact of an *Ar*-ion on *Cu*(001). Now we are interested in the evolution of the surface morphology after a low dose of ion bombardment. This is done using another numerical method called the kinetic Monte Carlo (KMC) method which is a special variant of ordinary Monte Carlo (MC). MC refers to a broad class of algorithms that solve (physical) problems by using random numbers. They were first used in the late 50s when electronic computers became available. The name MC is referring to the gambling at Monte Carlo, Monaco. In the 60s researchers began to develop a MC algorithm for computing the temporal evolution of systems from one state to another. In the 90s this approach became known as the KMC method. With this technique we can describe the diffusions of adatoms on the surface very well by exploiting the fact that the long-time dynamics typically consists of diffusions from one 4FH-site to the next. Instead of following the trajectory of this adatom through every vibrational period, the diffusions can be treated directly which enables us to reach vastly longer timescales than in MD. Every diffusion event occurs with a certain rate, which is exponentially proportional to its activation barrier height (for metals these are typically a few tenth of an *eV*). In this manner we can describe all possible diffusion effects. Thus we can follow the evolution of the surface for a given time using KMC.

In this chapter we discuss the results of our KMC simulations. We will briefly discuss the KMC model with which we describe the diffusions on the surface. Then we will present the results of two models: a very simple model according to the approaches described in chapter 1 and a more advanced model based on our results of the MD simulations.

3.2 Simulation Method

Diffusion

As described before in chapter 2, atoms oscillate in a potential well created by the neighbouring atoms. Depending on the amount of kinetic energy (which depends on the substrate temperature) an atom has the probability to cross the energy barrier between its current 4FH-site and its neighbouring 4FH-site. This is called a diffusion. Now the rate for this "hopping" from one 4FH site to the next is described by the equation:

$$h(E_B, T) = \nu_0 \times \exp(-E_B/k_B T) \quad (3.1)$$

where $h(E_B, T)$ is the diffusion frequency of an atom (in units of hops per second), ν_0 is the oscillation or attempt frequency of an atom inside a potential well (this frequency is only weakly temperature dependent and is therefore taken as a constant 10^{13}), k_B is the Boltzmann constant, T the temperature and E_B is the

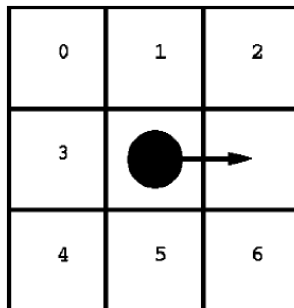


Fig. 3.1: The activation energy barrier for diffusion depends on the occupation of the NN - (1, 3 and 5) and NNN - (0, 2, 4 and 6) sites.

activation barrier of the diffusive move. The activation energy barrier E_B depends on the local environment of the hopping atom (i.e. the configuration of occupied and unoccupied adjacent sites).

For intralayer diffusion (diffusion on a layer), the activation energy depends mainly on the occupation of the NN - and NNN -sites. From this we can see that only 7 occupied / unoccupied sites can make a major contribution to the activation energy (see figure 3.1). These 7 atoms give $2^7=128$ possible configurations. Removing the symmetrical equivalents, we are left with 72 unique configurations with their unique energy barrier (a complete list can be found in table I [11]. We do not include concerted moves or exchange hopping. These are rarely occurring on $Cu(001)$ [11].

For interlayer diffusion (diffusion to a layer beneath), two possible paths are implemented. Diffusion over a (100) step edge and diffusion over a (110) step edge. Both interlayer diffusions have different activation barriers than their intralayer counterparts. This was solved by adding an extra barrier (an Ehrlich-Schwöbel barrier) to the equivalent intralayer energy barrier. For a (100) step edge we use $10meV$ extra and for a (110) step edge we use $60meV$.

To simulate in a reasonable amount of time, we have to scale the energy barriers. Diffusions with very low energy barriers take a lot of CPU-time although they do not really contribute to the final morphology. An example of these diffusion processes are for example the atoms that move forward and backward next to a step edge. To compress the range of diffusion rates we scale up the low diffusion barriers using relation:

$$E' = \begin{cases} E + \alpha(400meV - E) & \text{if } E \leq 400meV \\ E & \text{if } E > 400meV \end{cases} \quad (3.2)$$

where E is the activation energy barrier from the table and E' is the energy barrier that is scaled up by a constant α . Both the speed and the simulation results depend strongly on α . Higher values for α lead to more (110) step edges in the final morphology. In the results presented here we used $\alpha = 65\%$.

The interested reader is referred for more details about the KMC-algorithm used here to [25].

Sputtering

Sputtering events occur very rare compared to diffusion events. The starting velocity for an incoming Ar -ion of $800eV$ is about $15000 m/s$. Only within approximately $1nm$, the surface can have a relevant influence on an incoming ion. This distance takes the incoming Ar -ion only $0.02ps$. Using relation 3.2 we find that only diffusion steps with up to an energy of $0.040eV$ are enabled in this timescale. All diffusive moves with such low energy barriers occur instantaneously when possible and are all practically irreversible. Therefore, we make the approximation that during the impact there is no diffusion. In all simulations we perform normal incidence sputtering. To be able to compare with experiments, we sputter for 0.05 MLE.

3.3 Simple sputter model

The first sputter model we use in our KMC simulations is the most simple model that is possible for a sputtering event (see also 1.2.1). We draw a random number for the position on the surface where the ion will hit. At this position we remove one atom, creating a monovacancy.

In figure 3.2 we show the results of the simulations for various temperatures. We increased the temperature from 200 to 325K with steps of 25K. A single black dot represents a monovacancy. A vacancy cluster is represented by a black spot. For increasing temperatures we see the density of vacancy clusters decreasing. The cluster size increases. This is caused by the higher diffusivity of monovacancies at higher temperatures (see also section 1.4). In figure 3.2(c) we can also see a monovacancy in a vacancy cluster. These features can also be found for higher temperatures, they are however very rare. For high temperatures (see figure 3.2(f)) the large clusters are gone. This is a strange effect that is not in agreement with experiments performed on *Ag* [8] and *Cu* (see chapter 4). This effect is caused by the rescaling of the energy barriers using relation 3.2 and is especially caused by the diffusion processes 102 and 127 (see figure 3.3). The energy barrier for vacancy annihilation (process 102) is according to table I in [11] $E_{102} = 0.050eV$. Rescaling the energy barrier gives us a much higher energy barrier ($E'_{102} = 0.278eV$). The energy barrier for vacancy creation (process 127) has an energy barrier of $E_{127} = 0.280eV$. Rescaling gives us an energy barrier of $E'_{127} = 0.358eV$. Because of the fact that these energy barriers get closer to each other, the processes get more competitive. This causes the physical unrealistic effect of spontaneously created monovacancies that results in monovacancies that are not able to form a cluster anymore at higher temperatures. We can conclude that we need to improve the set of energy barriers that is used to reproduce reliable results for sputtering.

If we therefore perform a simulation at 250K for higher fluence we can clearly see that this very simple model is in agreement with inverse homoepitaxial deposition [8]. Notice that this comparison is with homoepitaxial deposition at a much lower temperature (see also figure 1 in [8]). The fact that this sputtering model gives results comparable to inverse homoepitaxial deposition is the result of this model. The patterning is close to a checkboard pattern in the [110] direction. The remaining adatom islands have elongated shapes in all directions and are connected to each other.

3.4 Advanced sputter model

The simulations in chapter 2 as well as experiments indicate that an *Ar*-ion creates on impact a similar number of vacancies and adatoms. A more advanced sputter model would also include adatom creation. The most simple model for this is to pick an atom at a random position on the surface, then remove this atom and find a stable location for it in on top of one of the NNN positions by drawing a random number. This results in a adatom vacancy recombination of 25%.

The results of the temperature dependence of low fluence simulations are shown in figure 3.5. Now that we create adatoms we need more colors in the image. Monovacancies are again represented by black dots, the initial height of the surface is gray and the adatoms are white.

Figure 3.5 shows as in the previous sputter model, that at temperatures up to 250K for increasing temperature the vacancy cluster density decreases and the vacancy cluster size increases. At higher temperatures we see also recombination of adatoms and vacancies. This results in a decreasing adatom- and vacancy coverage for increasing temperature. This effect may be caused by the high probability for the created adatom to recombine with the vacancy. The very low Ehrlich-Schwöbel barrier for diffusion over the (100) step edge is very easy to overtake. The results of the MD simulations in chapter 2 show us that the adatom has a distance of 10-25 Å from the point of impact. The single adatoms might quickly cluster and form a stable adatom cluster, preventing the adatoms to recombine with vacancies.

In figure 3.6 we present the resulting morphology of a simulation performed at 250K for higher fluence. The patterning is not a regular structure anymore as it was for the simplest approach. The remaining adatom islands however are separated from each other. This can be explained by the quick clustering of atoms to produce stable adatom clusters.

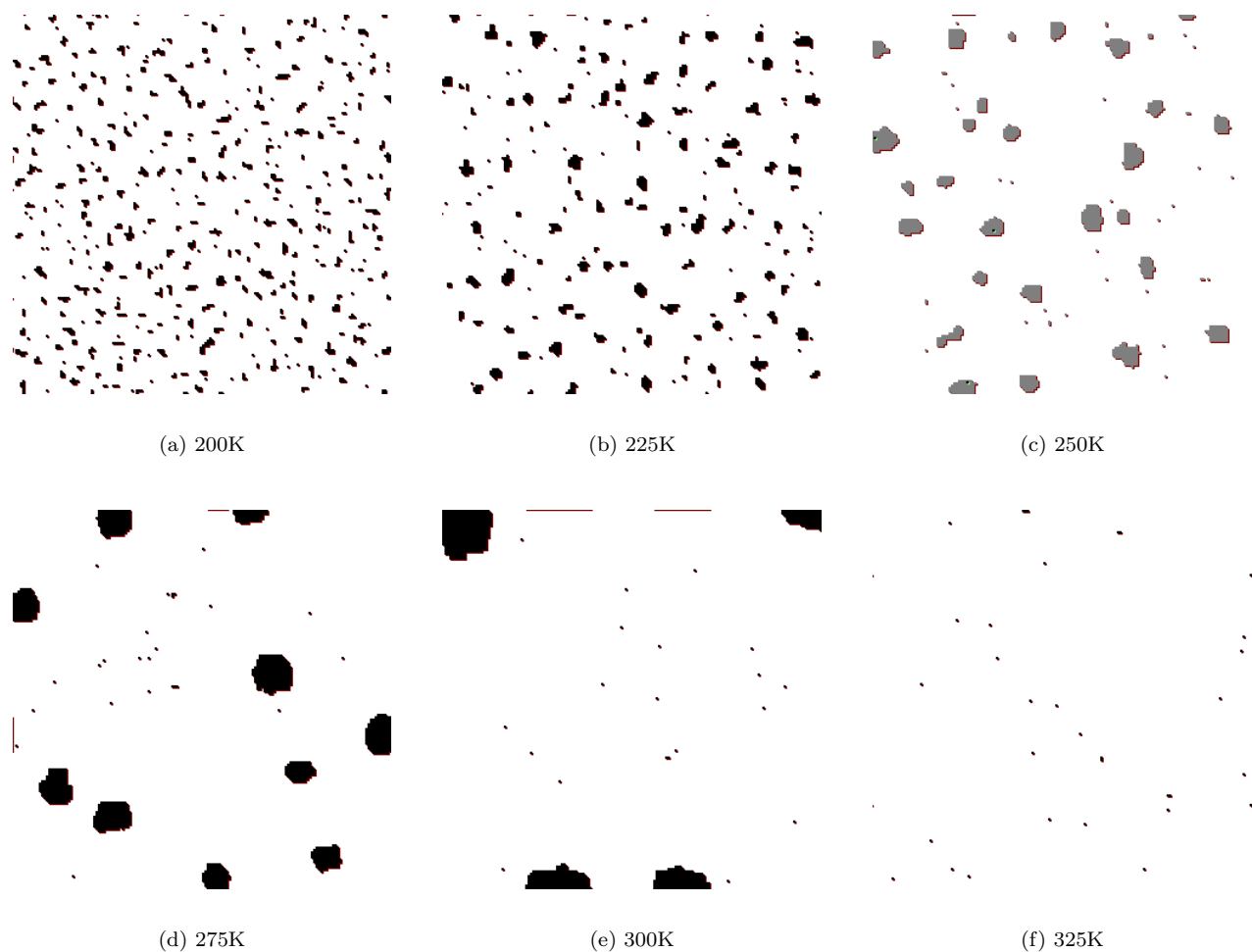


Fig. 3.2: Surface morphologies for increasing temperatures using a impact-model where one impact creates one monovacancy. The ion dose is 0.05 MLE/min. The snapshots are after 1 minute. Size 160×160 atoms ($410 \times 410 \text{ \AA}^2$).

3.5 Conclusion

We used two very simple sputter models for the *Ar*-ion impact that resulted into different evolutions of the *Cu*(001) surface morphology using a KMC algorithm that makes use of the rescaled energy barriers of Biham [11]. The results found are highly temperature dependent. Due to the rescaling of the energy barriers e.g. vacancy annihilation and creation gets physical unrealistic competitive. This prevents monovacancies for higher temperatures to form a cluster. In order to get physical realistic results, we should improve the set of energy barriers and improve the model for the *Ar*-ion impact. We propose a model in which a *Ar*-ion creates six vacancies in a cluster and four adatoms which are randomly spread over an area between a radius of 10 and 25 Å. The sputtering yield will then be two atoms per ion. These values are in agreement with a "head-on-head" 800eV *Ar*-ion impact on *Cu*(001) found using MD (see also table 2.2). The next step would be to include statistics on the position of impact.

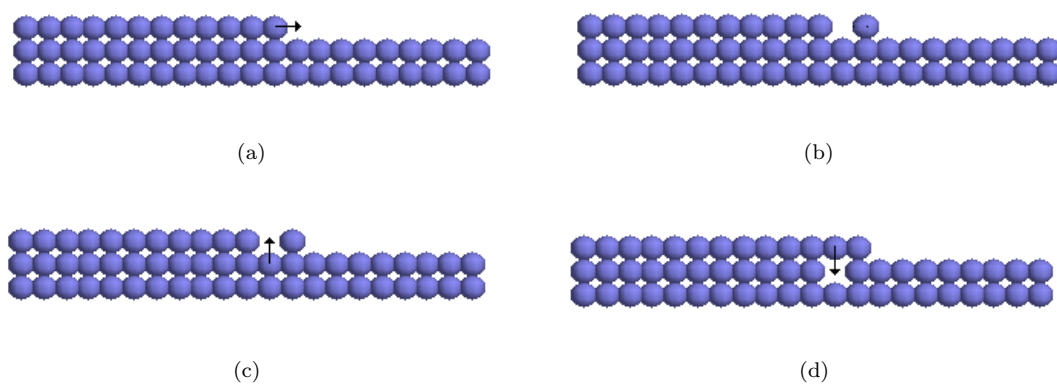


Fig. 3.3: Two competitive processes that play a fundamental role in the evolution of the surface morphology after a low dose of ion bombardment. (a & b) Step edge diffusion and (c & d) vacancy creation and annihilation. View is on top of the surface.

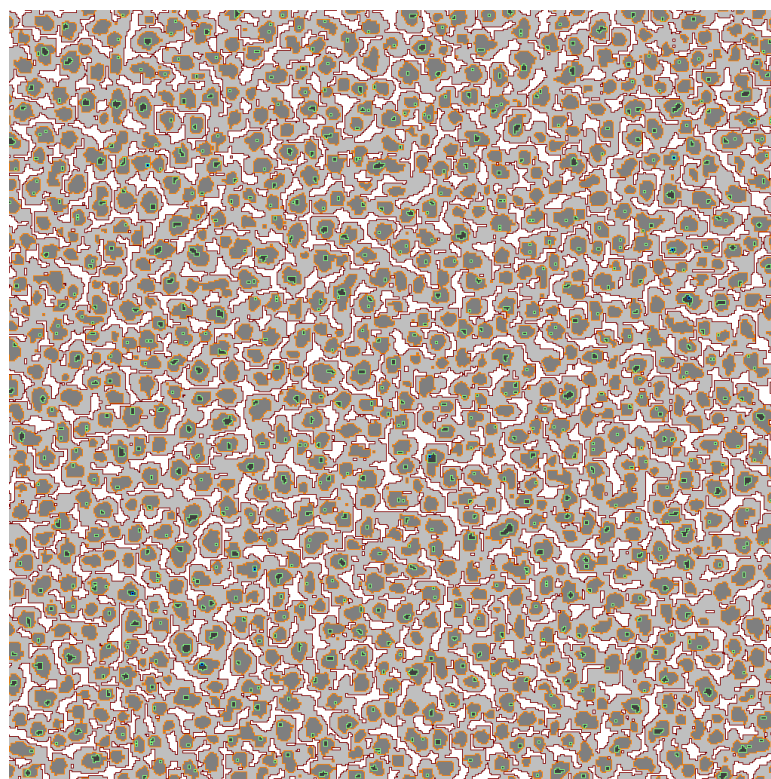


Fig. 3.4: Surface morphology for using a impact-model where one impact creates one monovacancy. The ion dose is 1 MLE/min. The snapshot is after 1 minute at 250K. Size 512×512 atoms ($1306 \times 1306 \text{ \AA}^2$).

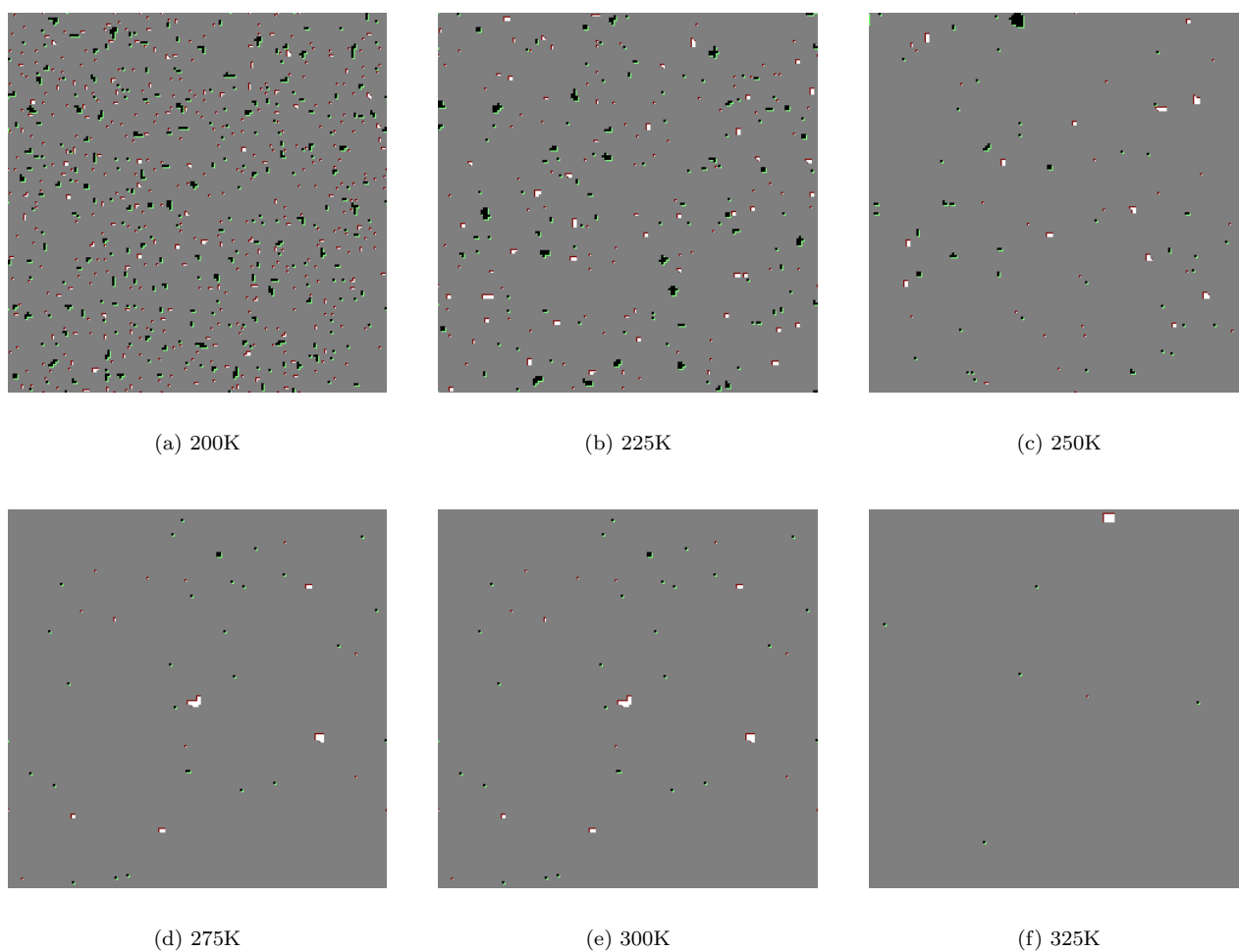


Fig. 3.5: Surface morphologies for increasing temperatures using a impact-model were one impact creates one monovacancy and one adatom in the NN-4FH site. The ion dose is 0.05 MLE/min. The snapshots are after 1 minute. Size 160×160 atoms ($410 \times 410 \text{ \AA}^2$).

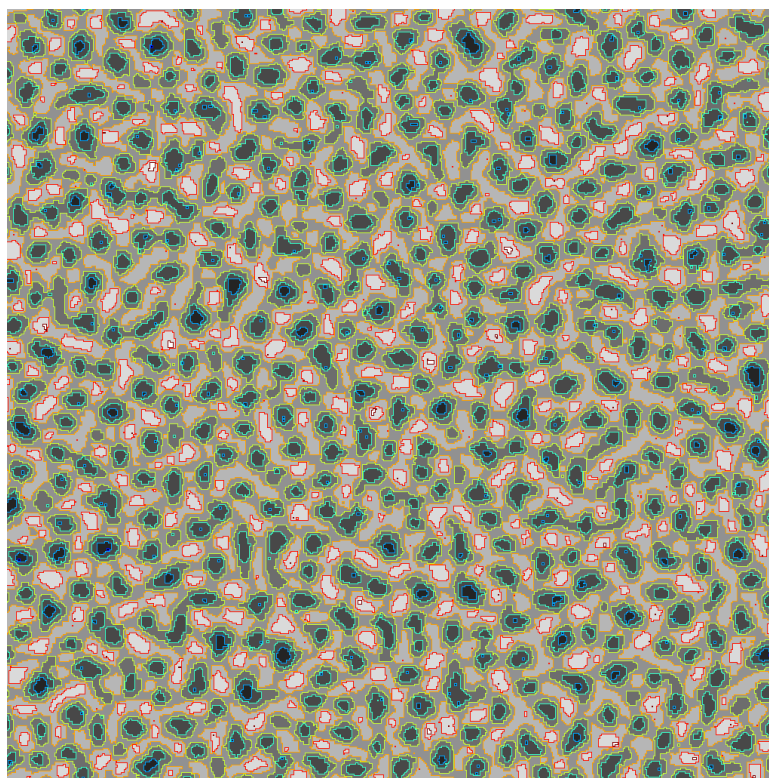


Fig. 3.6: Surface morphology for using a impact-model where one impact creates one monovacancy. The ion dose is 1 MLE/min. The snapshot is after 1 minute at 250K. Size 512×512 atoms ($1306 \times 1306 \text{ \AA}^2$).

Experimental results

4.1 Introduction

Now that we brought our theoretical model "to life" we are able to compare it's results with experiments. Studies concerning single ion impacts of $1keV Ne^+$ on $Ag(001)$ [8] and $40eV-5keV Ne^+$, Ar^+ and Xe^+ on $Pt(111)$ [26] have already been performed and reported. The adatom and vacancy clusters were found to be of mono-atomic height. On $Ag(001)$ a single ion impact creates on average one vacancy cluster of about 8-10 monovacancies surrounded by 3-4 adatom clusters of 6-7 atoms each.

To analyse single ion impacts and sputtering yields we need a microscopy technique to visualize the surface morphology after ion bombardment. Scanning probe techniques are such techniques and they are used in surface science to produce a real space image of a surface. Our method of choice is the Scanning Tunneling Microscope (STM). In this chapter we discuss the use of the STM to determine surface defects after normal incidence Ar -ion erosion on a $Cu(001)$ surface. By scanning after a low dose irradiation of an atomically flat surface at low temperatures where surface diffusion is absent, single impacts are observable, which consists of a crater surrounded by (some) adatom clusters.

Before we discuss the results we will briefly discuss the experimental details in which these results were observed and the STM technique.

4.2 Experimental

Setup

All the experiments are performed in an ultra-high vacuum (UHV) set-up which has a base pressure of $2 \times 10^{-10} mbar$. Attached to the UHV chamber we have several instruments which allow us to perform in-situ measurements. The ones we use for the experiments described here are:

- Ion sputter gun: Used for cleaning and patterning the sample. It is possible to vary the energy up to $2keV$.
- Auger Electron Spectroscopy (AES): Used for the chemical analysis of the sample.
- Quadrupole Mass Spectroscopy (QMS): Used for analysing the rest gases in the UHV chamber.
- Manipulator: Used to transport the sample into the right position for analysis or sputtering.
- STM: For analysing the surface-morphology after ion bombardment.

A photograph of the UHV set-up is shown in figure 4.1.

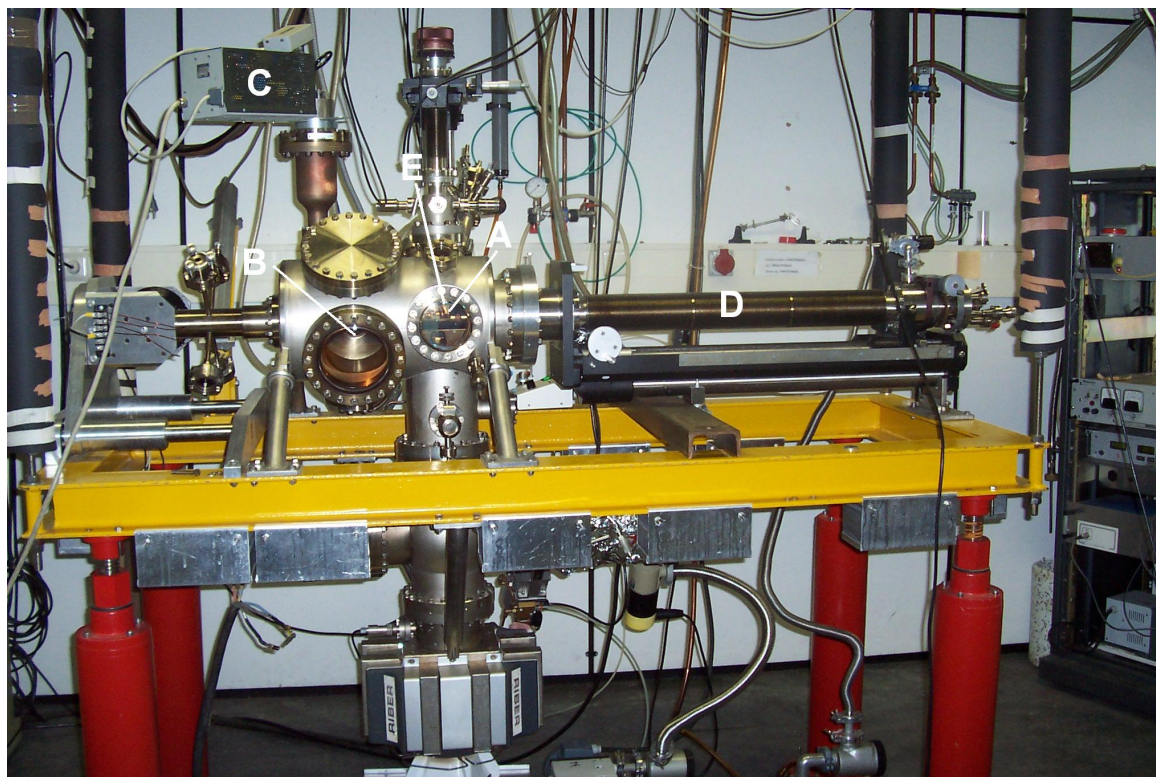


Fig. 4.1: Photograph of the UHV set-up used in the experiments. The upper part contains the sample and all instruments. The pumps are located at the lower part. The ion sputter gun (a) and the AES (b) are located at the back. QMS (c), manipulator (d). The STM (e) is located just above the sample.

Sample preparation and experimental procedure

The sample used in these experiments is a monocrystalline *Cu*-sample. The fcc-crystal is cutted in the (001) direction with an accuracy of $< 0.1^\circ$. The sample is mechanically polished and heated to 1300K in a H_2 environment for a few days. This results in a very low impurity level of sulphur being the main bulk contaminant. After mounting the sample in the UHV chamber, further cleaning is needed. This is accomplished by successive cycles of sputtering with 800eV *Ar*-ions at room temperature (RT) followed by annealing at 800K for 10 minutes. This procedure results in a clean surface with a contamination level below the AES detection limit. However, in the AES analysis not all contaminations are detected (due to the fact that they are very small and cover only a small fraction of the surface and the fact stepedges are pinning at the contaminations). To make sure the sample is clean we use the STM. The starting point, prior to typical erosion experiment, is a contamination free surface which exhibit large flat terraces (see figure 4.2).

All the experiments are performed at normal incidence. The ion flux is calibrated using the Faraday cup and amounts a current density of $0.16\mu A/cm^2$. This is equivalent with an ion flux of $1 \times 10^{12} ions/cm^2s$. In this thesis we express the ion dose in monolayer equivalent (MLE) where one MLE is numerically identical with the atomic density of *Cu* atoms in the (001) plane ($1.53 \times 10^{15} atoms/cm^2$). After sputtering at the desired fluence, the sample is quenched to 110K to suppress diffusion processes at this low temperature. The resulting surface morphology is investigated with the STM.

STM

The surface morphology after a typical sputtering experiment is investigated using the STM. The STM makes use of the quantum mechanic tunneling effect. By moving an atomically sharp tip over the surface (see figure

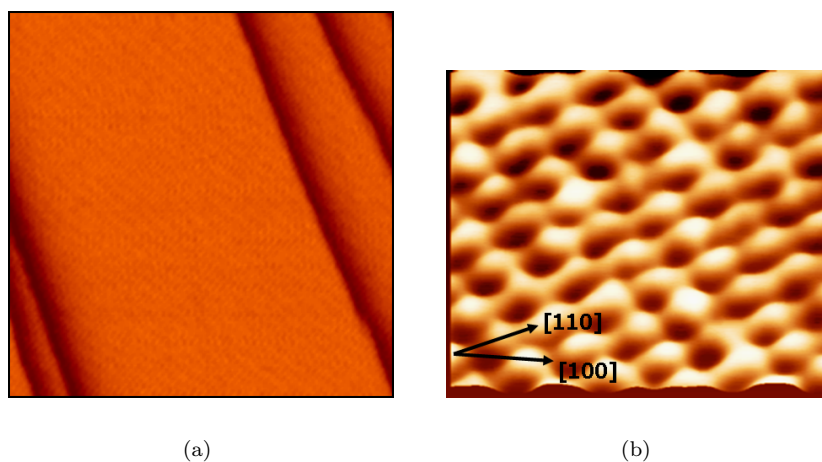


Fig. 4.2: (a) STM image of a flat $Cu(001)$ surface. Scansize $85 \times 85nm^2$. The tunneling current is $0.2nA$ and the tunneling voltage is $0.43V$. (b) Atomic resolved STM image of $Cu(001)$. The tunneling current is $2nA$ and the tunneling voltage is $0.13V$. Here the $[100]$ and $[110]$ directions can be distinguished.

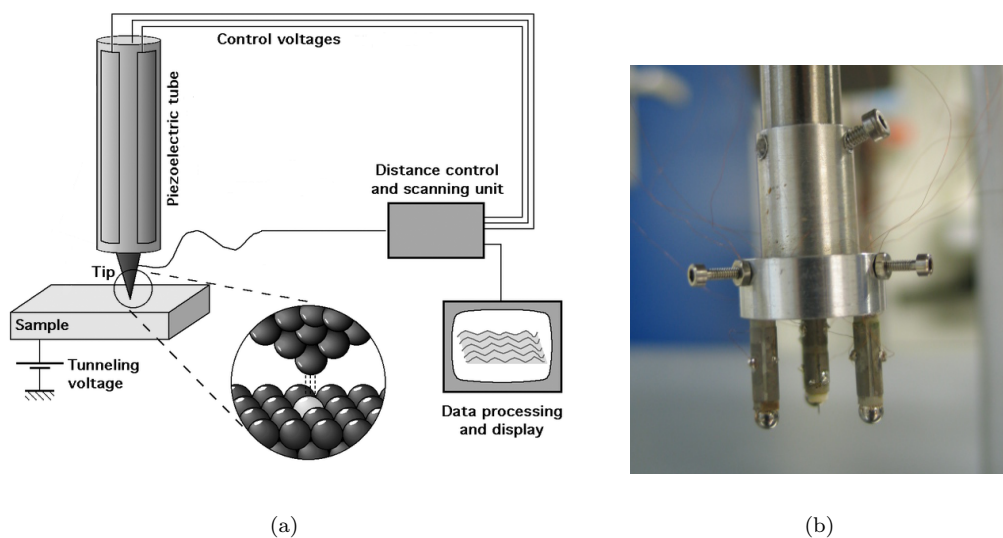


Fig. 4.3: (a) Schematic overview of a STM. Taken from Michael Schmid, TU Wien. (b) The "homebuilt" inverse Beetle-type STM used in our experiments [27].

4.3) the wave functions of the atom at the tip overlap with those of the probed surface. If a bias voltage between the tip and the sample is applied, a net current will result. This current is exponentially dependent on the tunneling gap between the tip and surface. Therefore the STM has an extremely high vertical resolution.

The small tunneling current is amplified and is then taken over by the feedback loop which has the purpose of keeping a constant tunneling gap between the tip and the surface. The feedback loop compares the measured current with the setpoint and depending on the results of this test, it will send appropriate voltages to the piezo (to expand or contract) so that the gap is maintained at a constant value. Monitoring the voltages that are applied to the piezo while scanning over a surface gives a direct topographical image of the surface. This mode

of scanning is known as "constant-current mode".

From 1965 to 1971 Russel Young developed an apparatus build on the idea of the tunneling current combined with a scanning device. The difficult problems in the mechanical design (to find a adequate way to isolate the instrument for vibrations) were solved by Gerd Binnig and Heinrich Rohrer. They shared in the Nobel Prize in Physics in 1986 for their design of the STM [28]. They were the first to observe atomic resolution on $Si(111)$.

In our set-up we use a modified version of the inverse Beetle-type STM [29] that makes use of outer piezos for the approaching and inner piezo for scanning (see figure 4.3(b)). A tungsten tip has been used for the measurements in UHV. We produce this tip by electro-chemical etching. Sometimes we improve the quality of the tip during scanning using the "soft crash"-method. We scan in constant-current mode.

4.3 Single ion impacts

In order to resolve single ion impacts we have to perform experiments with very low fluence and a low temperature so that diffusions will not effect the final morphology. We performed experiments at 200K for an ion dose of 0.001MLE (see figure 4.4). In this image three vacancy clusters and four adatom clusters are visible. So roughly one single ion impact produces one or two adatoms islands. The adatom cluster size is 45\AA^2 which corresponds to about 7 atoms. The vacancy cluster is 42\AA^2 which corresponds to 6-7 missing atoms.

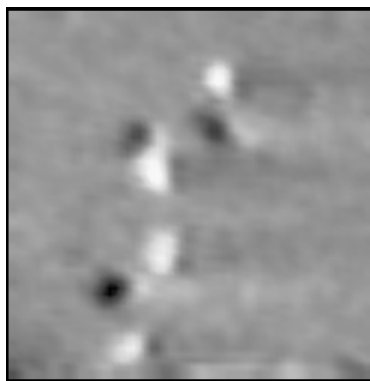


Fig. 4.4: STM topograph of $Cu(001)$ obtained after irradiation at 200K with $800eV Ar^+$ and an ion fluence of 0.001MLE. Scansize $87 \times 87 \text{\AA}^2$.

From the adatom- and vacancy coverage we can calculate the sputtering yield using the relation:

$$Y_{sp} = \frac{\theta_{vac} + \theta_{bulk} - \theta_{ad}}{\theta_{ion}} \quad (4.1)$$

Our calculations lead to a negative sputtering yield. Negative sputtering yields are however physically unrealistic. The STM topograph is a result of the convolution between the STM tip and the surface structure. Therefore the adatom clusters will be overestimated while vacancy clusters will be underestimated (see figure 4.5). The convolution effect will give a major contribution to the underestimated sputtering yield. Moreover, using the STM it is also impossible to measure bulk vacancies, which are still trapped under the surface at this low temperature. The last point of discussion is the fact that small vacancy clusters and monovacancies can not be resolved by the STM (see also [12]). Therefore the vacancy coverage will be underestimated, leading to a negative sputtering yield.

In conclusion, we have some major errors in determining the real coverages for adatom- and vacancy clusters. This results in a problem for calculating the sputtering yield. However, we can overcome this problem by performing experiments at higher temperatures with higher ion doses. At higher temperatures the convolution effect will be diminished by minimizing the edge area of the cluster. We also expect the bulk vacancies to anneal to the surface and thereby they will become visible to the STM as surface vacancies. Small vacancies will nucleate easier to bigger vacancy clusters and are easier to be imaged.

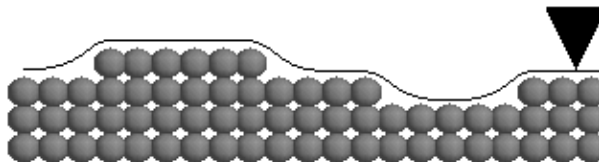


Fig. 4.5: The convolution effect. Adatom island will be overestimated and vacancy islands underestimated due to the convolution between sample and STM tip.

4.4 Temperature dependence

In order to diminish the strong convolution effects we perform higher fluence experiments at higher temperatures. We increase the temperature from 200 to 325K with increments of 25 degrees using an ion fluence of $\theta_{ion} = 0.05$ MLE. From the images, the coverage of adatoms (θ_{ad}) and vacancies (θ_{vac}) can be inferred. We can then calculate the sputtering yield using relation 4.1. If we compare this equation with equation 4.1 in chapter 2 we did not include interstitials and bulk vacancies. Since interstitials are not stable at these temperatures we expect them to be annealed at the surface. We do not expect subsurface vacancies to be stable at higher temperatures.

The results of the coverages for adatom- and vacancy clusters are shown in figure 4.7. We can only calculate a sputtering yield for higher temperatures where the convolution error is diminished and the bulk vacancies are annealed. For 325K we find (using relation 4.1) a sputtering yield of 0.2 atom per ion.

4.5 Conclusion

In order to analyse single ion impacts we perform experiments using a low ion dose and low temperatures. Using the STM we resolve for low fluence that one single *Ar*-ion impact on *Cu*(001) creates on average one vacancy cluster of about 6-7 monovacancies and 1-2 adatom cluster of about 7 atoms. The conservation of mass will lead to a negative sputtering yield, which is physical unrealistic. However, the sputtering yield can also be determined from experiments at high temperatures and higher ion doses. These experiments result in a sputtering yield of about 0.2 atoms per ion at 325K. Unfortunately this value is one order of magnitude lower than in previous studies [30] where it is found to be about 1.8 atoms per ion. This can be explained by the systematic error due to the (diminished but still present) convolution effect or by the possible existence of deeper bulk vacancies. Previous studies about *Ar* desorption on *Cu* reveal the existence of such trapped vacancies which are mobile at 700K [31].

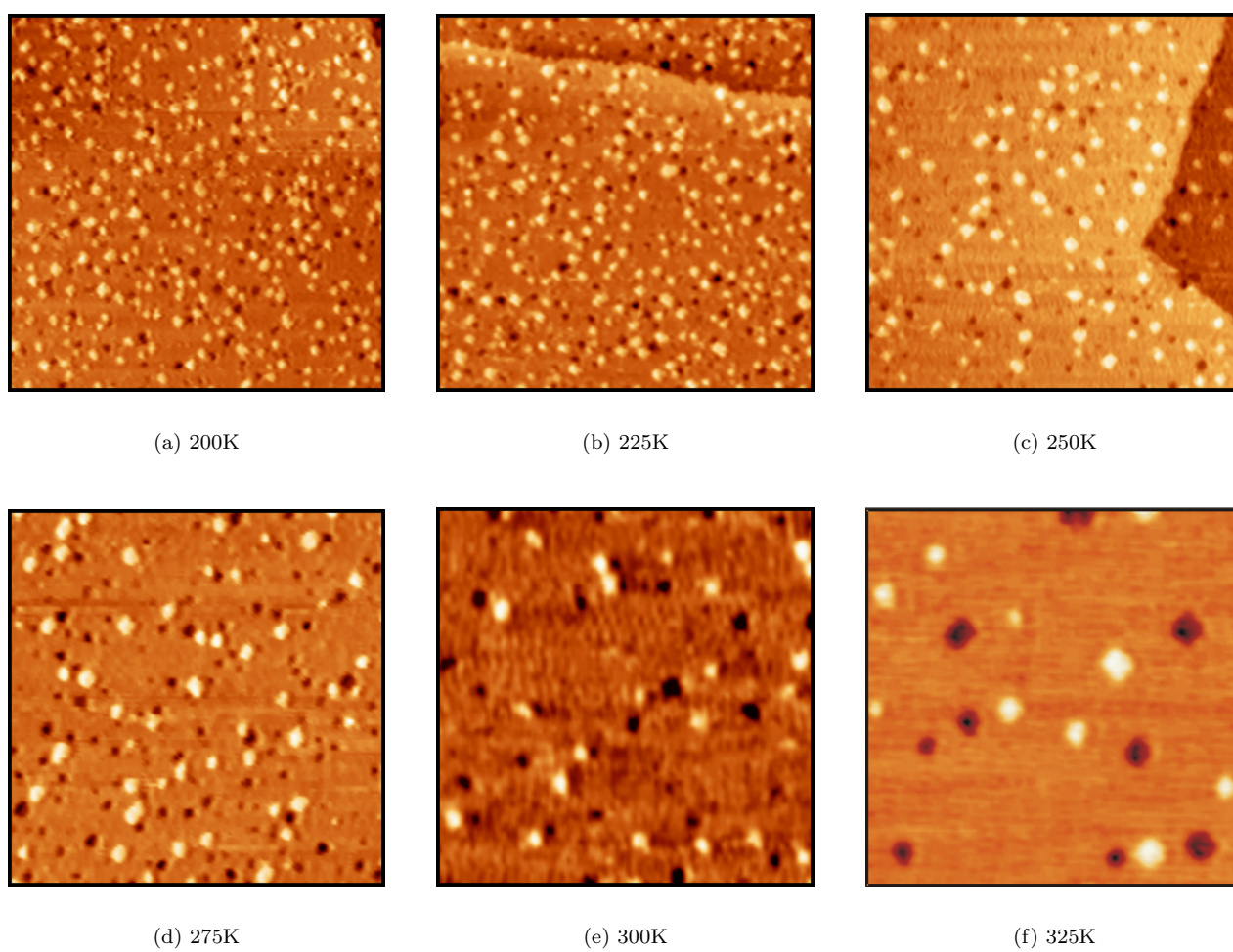


Fig. 4.6: STM topographs of $Cu(001)$ obtained after irradiation with a 0.05 MLE dose of 800eV Ar -ions at different temperatures. All figures have a scansize of $410 \times 410 \text{ \AA}^2$.

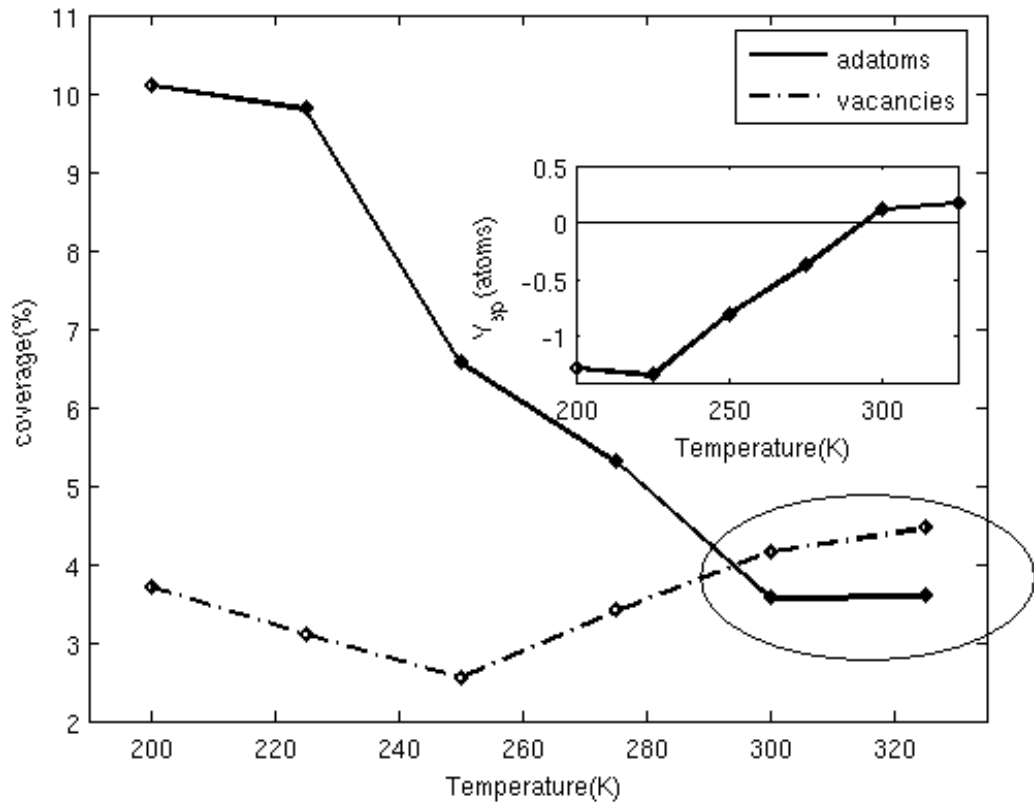


Fig. 4.7: Coverages found for adatom- and vacancy islands for various temperatures. In the inset we present the calculated sputtering yields using these coverages.

Conclusions

At the end of this report it is time to reflect and compare the simulations to the experiments we performed. We compare and discuss the sputtering yield and the adatom- and vacancy clusters found for both experiments and simulations. At the end we will make some recommendations for further research.

Sputtering yield

In chapter 2 we used MD to find values for the sputtering yield, adatom yield, yield for interstitials and the yield for surface- and bulk vacancies after the impact of an *Ar*-ion on the *Cu*(001) surface. For the random impact we found a sputtering yield of about 3-4 atoms for temperatures up to 150K. For a higher temperature the sputtering yield increases. The sputtering yield determined from experiments (described in chapter 4) at high temperatures and higher *Ar*-ion doses on *Cu*(001) is of about 0.2 atoms per ion. Previous studies [30] found a sputtering yield of about 1.8 atoms per ion.

The sputtering yield determined by performing MD is too high. This can be caused by the potential we use. The potential used in the MD simulations has a correct cohesive energy for *Cu*, but the melting temperature and energy for creating a vacancy are not in agreement with the values found for *Cu* experimentally. This may result in a unphysical large amount of vacancies, which in turn can lead to an overestimated sputtering yield. We also neglected long-range interactions. These might re-attract sputtered atoms with a very low kinetic energy to the surface and create adatoms on the surface.

On the other side, the sputtering yield found in the performed experiments is too low. This can be explained by the systematic error due to the convolution effect that leads to overestimated adatom clusters and underestimated vacancy clusters. We will however not be able to rule out the convolution effect, we can only diminish it. The other explanation for the low sputtering yield found may be the existence of subsurface vacancies that are deeper in the bulk. Previous studies [31] reveal the existence of trapped subsurface vacancies that become mobile at higher temperatures than the ones we use in our experiments.

Adatom- and vacancy clusters

MD is used to simulate the impact of a 800eV *Ar*-ion on *Cu*(001). The adatom yield is found to be about 2-8 atoms for temperatures up to 150K. The vacancy yield is found to be 4-8 missing atoms. Bulk vacancies created are rare, but can be created at impact. Interstitials are created but are almost immediately annealed to the surface. For higher temperatures we have difficulties in categorising. Using the STM we resolve for low fluence that one single *Ar*-ion impact on *Cu*(001) creates on average one vacancy cluster of about 6-7 monovacancies and 1-2 adatom cluster of about 7 atoms each. These values are in the range of the values found by MD. However, the spreading of the adatoms in MD is much larger and they do not form an adatom cluster within the first 5ps after impact. These single adatoms have however a high diffusivity and can cluster due to their random walks on the surface. To calculate the evolution of the surface morphology after a low dose of ion bombardment

we make use of a KMC algorithm in chapter 3. Monovacancies created by a single ion impact will diffuse and form larger vacancy clusters. For higher temperatures this diffusion is faster and larger clusters are formed. The adatoms created in the more advanced model diffuse and form clusters. Therefore the re-arranging of the adatoms to a cluster may be in the order of nanoseconds while the forming of a vacancy cluster is in the order of picoseconds. This can be explained by the fact that the monovacancies are close together just after impact. The adatoms however can be seen as sputtered atoms that just did not make it. Due to their impuls of the *Ar*-ion they are squeezed out of the surface and they land about 10-25 Å from their initial position. The fact that vacancy clusters form faster than adatom clusters is in agreement with the values found for their diffusivity in chapter 1.

Recommendations

We already discussed the limitations of the MD algorithm developed for this project in section 2.4. By improving the potentials (e.g. by using available EAM-potentials) we can correct for the melting temperature and for the creation energy of a vacancy. The algorithm can also perform simulations for (almost) every other kind of material as long as the LJ-parameters ϵ and σ are known. Therefore we can use this algorithm for almost any kind of particle(s)-solid collision. The shape of the substrate and incoming particles is also very easy to modify since the algorithm makes use of a file containing the coordinates. In particular for the *Ar*-ion impact on *Cu*(001) we could study the defects created by grazing incidence and compare them to experiments [1]. This may give us a better understanding of the fundamental processes that play a role in these experiments.

For the KMC algorithm used in this thesis we need to include a better model for the single *Ar*-ion impact. Using a model for grazing incidence developed by MD simulations combined with an improved set of energy barriers for the *Cu*(001) surface, may enable us to study the atomic diffusion processes that play a fundamental role in nanopatterning. Since Biham [11] also listed the energy barriers for *Ag*, *Au*, *Ni* and *Pd* and there are also good EAM-potentials available for these metals [22], we are able to study these metals as well.

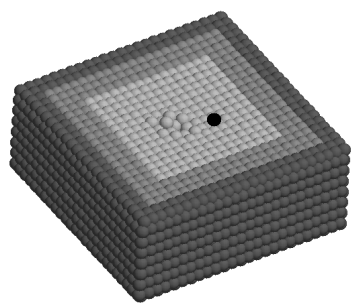
As one can see there is a whole zoo of phenomenon that we may get a better understanding of by performing MD or a combination of MD and KMC.

References and Notes

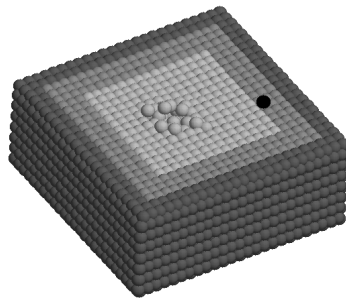
- [1] M. Ovsyanko, Ph.D. thesis, University of Twente, 2006.
- [2] C.-C. Hwang, J.-G. Chang, and S.-P. Ju, *Journal of the Chinese Society of Mechanical Engineers* **24**, 309 (2003).
- [3] A. Voter, in *Radiation Effects in Solids*, edited by K. Sickafus and A. Kotomin (Springer, Dordrecht, 2005), Chap. Introduction to the Kinetic Monte Carlo method.
- [4] R. Bradley and J. Harper, *Journal of Vacuum Science Technology A* **6**, 2390 (1988).
- [5] C. Teichert, Ph.D. thesis, Martin-Luther-Universität Halle-Wittenberg, 1992.
- [6] A. K. Hartmann and R. Kree, *Physical Review B* **65**, 193403 (2002).
- [7] P. Sigmund, *Physical Review* **184**, 383 (1969).
- [8] G. Costantini, F. B. de Mongeot, C. Boragno, and U. Valbusa, *Physical Review Letters* **86**, 838 (2001).
- [9] K. Oura *et al.*, *Surface science an introduction* (Springer, Berlin, 2003), page 371-372.
- [10] I. Furman and O. Biham, *Physical Review B* **62**, R10 649 (2000).
- [11] H. Mehl, O. Biham, and I. Furman, *Physical Review B* **60**, 2106 (1999).
- [12] R. v. Gastel *et al.*, *Surface Science* **512**, 10 (2002).
- [13] M. Basham, P. Mulheran, and F. Montalenti, *Surface Science* **565**, 289 (2004).
- [14] <http://home.student.utwente.nl/t.r.j.bollmann>.
- [15] M. Allen and D. Tildesley, *Computer simulation of liquids* (Clarendon Press, Oxford, 1987).
- [16] H. Berendsen *et al.*, *Journal of Chemical Physics* **81**, 3684 (1984).
- [17] Y. Hu and S. B. Sinnott, *Journal of Computational Physics* **200**, 251 (2004).
- [18] D. Frenkel and B. Smit, *Understanding Molecular Simulation* (Academic Press, San Diego, 2002).
- [19] T. Pang, *An introduction to computational physics* (Cambridge University Press, Cambridge, 2006).
- [20] C. Busse *et al.*, *Surface Science* **488**, 346 (2001).
- [21] F. Karetta and H. Urbassek, *J. Appl. Phys.* **71**, 5410 (1992).
- [22] S. Foiles, M. Baskes, and M. Daw, *Physical Review B* **33**, 7983 (1986).

- [23] Y. Mishin *et al.*, Physical Review B **63**, 224106 (2001).
- [24] K.-H. Muller, Physical Review B **35**, 7906 (1987).
- [25] T. Warnaar, Master's thesis, University of Twente, Enschede, 2006.
- [26] T. Michely and C. Teichert, Physical Review B **50**, 11 156 (1994).
- [27] P. Hegeman, Ph.D. thesis, University of Twente, 1998.
- [28] G. Binnig, Physical Review Letters **49**, 57 (1982).
- [29] K. Besocke, Surface Science **181**, 145 (1987).
- [30] H. Roosendaal, in *Topics in Applied Physics*, edited by R. Behrisch (Springer-Verlag, Berlin, 1981), Vol. 47, Chap. 5.3.1 a), p. 224.
- [31] M. Fluss *et al.*, Journal of Physics F: Metal Physics **10**, 1763 (1980).

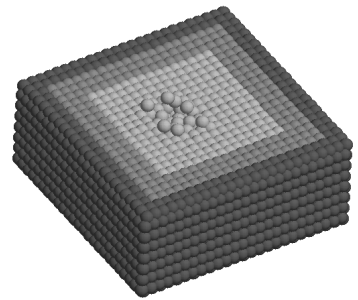
Appendix A



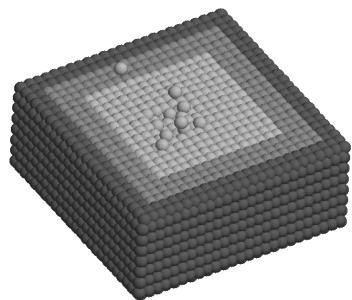
(a) $t = 250\text{fs}$



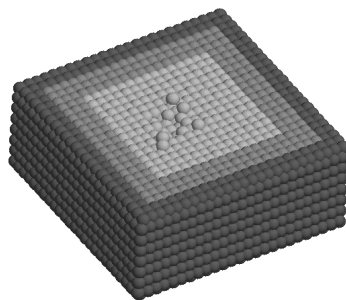
(b) $t = 500\text{fs}$



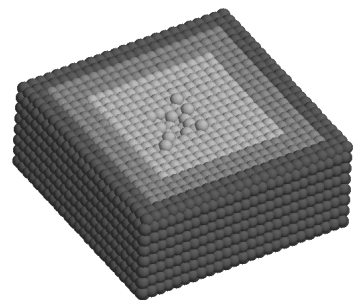
(c) $t = 750\text{fs}$



(d) $t = 2.5\text{ps}$



(e) $t = 3.5\text{ps}$



(f) $t = 5\text{ps}$

Fig. 1: Snapshots (3D) of a 800eV Ar -ion normal incidence impact on the $Cu(001)$ substrate at 1K.

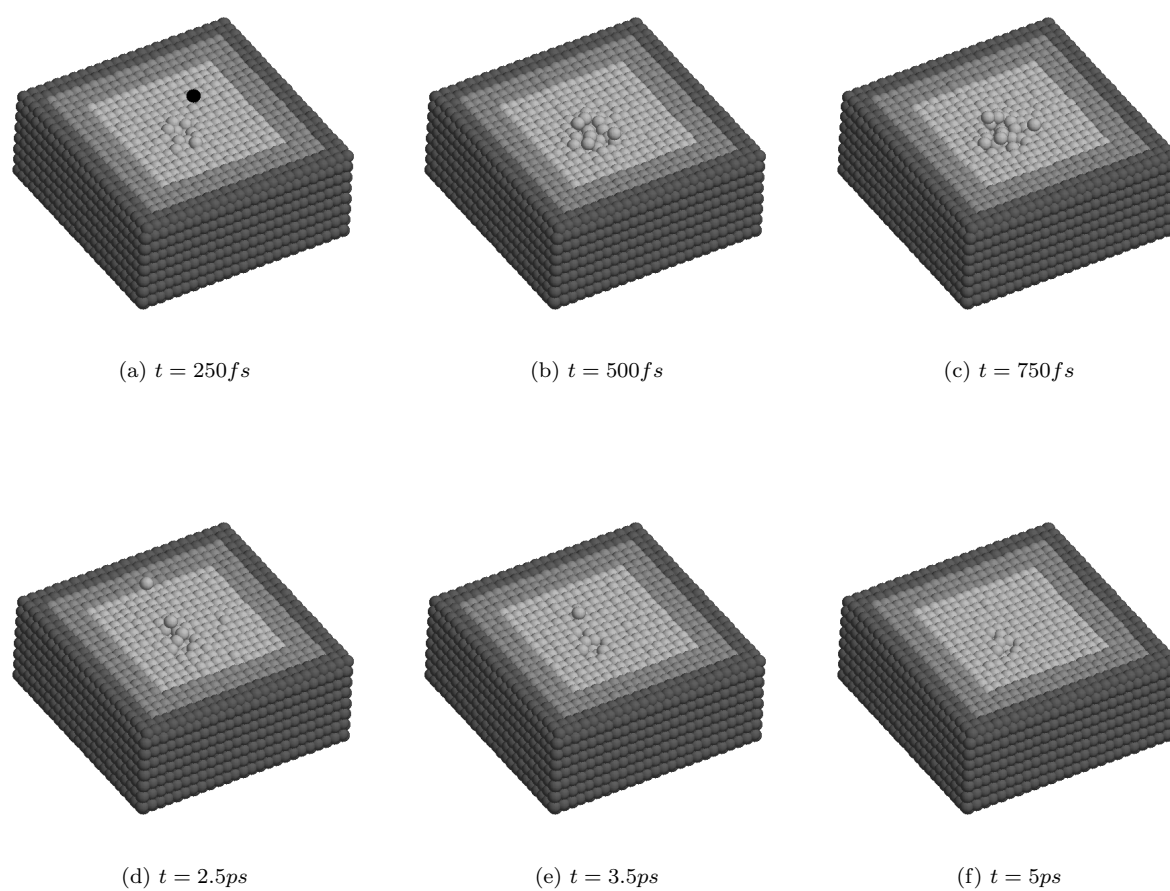


Fig. 2: Snapshots (3D) of a 800eV Ar^+ -ion normal incidence impact on the $\text{Cu}(001)$ substrate at 50K .

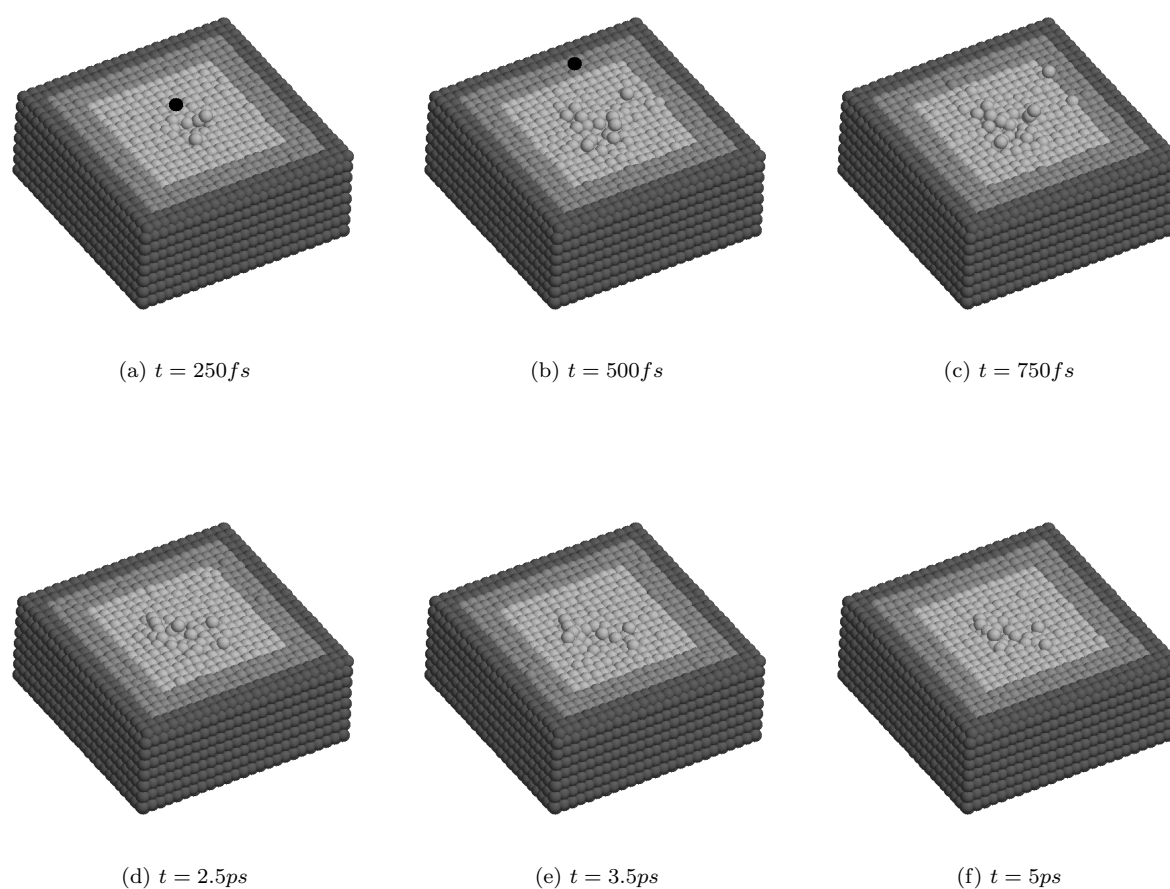


Fig. 3: Snapshots (3D) of a $800eV$ Ar -ion normal incidence impact on the $Cu(001)$ substrate at $100K$.

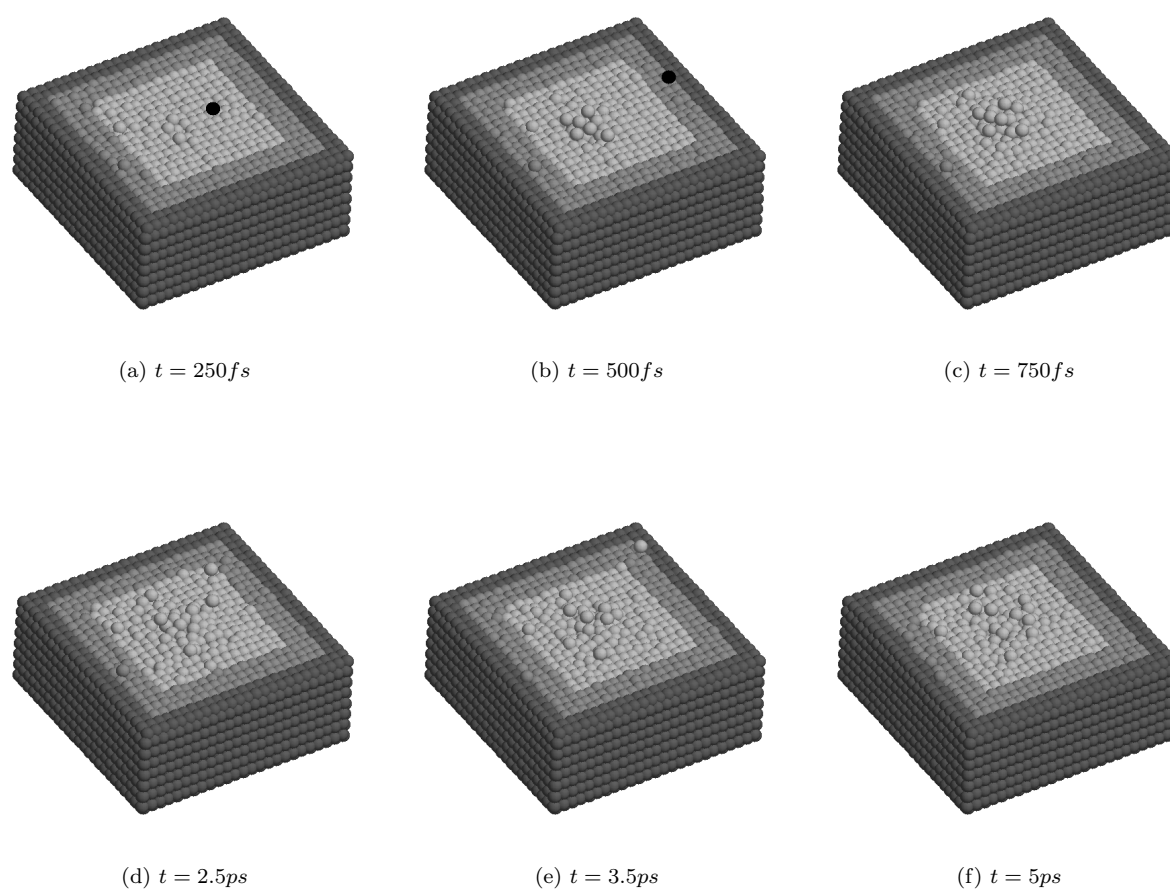


Fig. 4: Snapshots (3D) of a 800eV Ar -ion normal incidence impact on the $Cu(001)$ substrate at 150K .

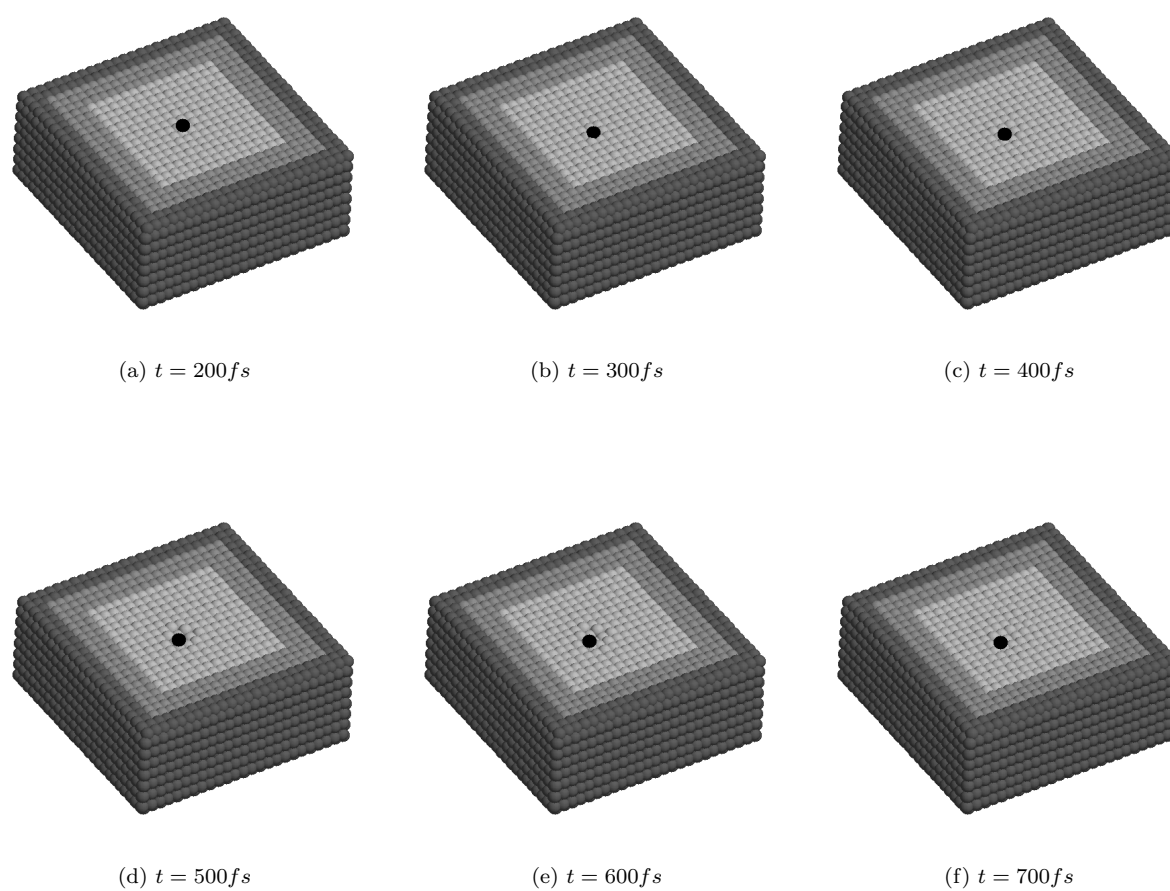


Fig. 5: Snapshots (3D) of a 100eV Ar^+ -ion normal incidence impact on the $\text{Cu}(001)$ substrate at 1K.

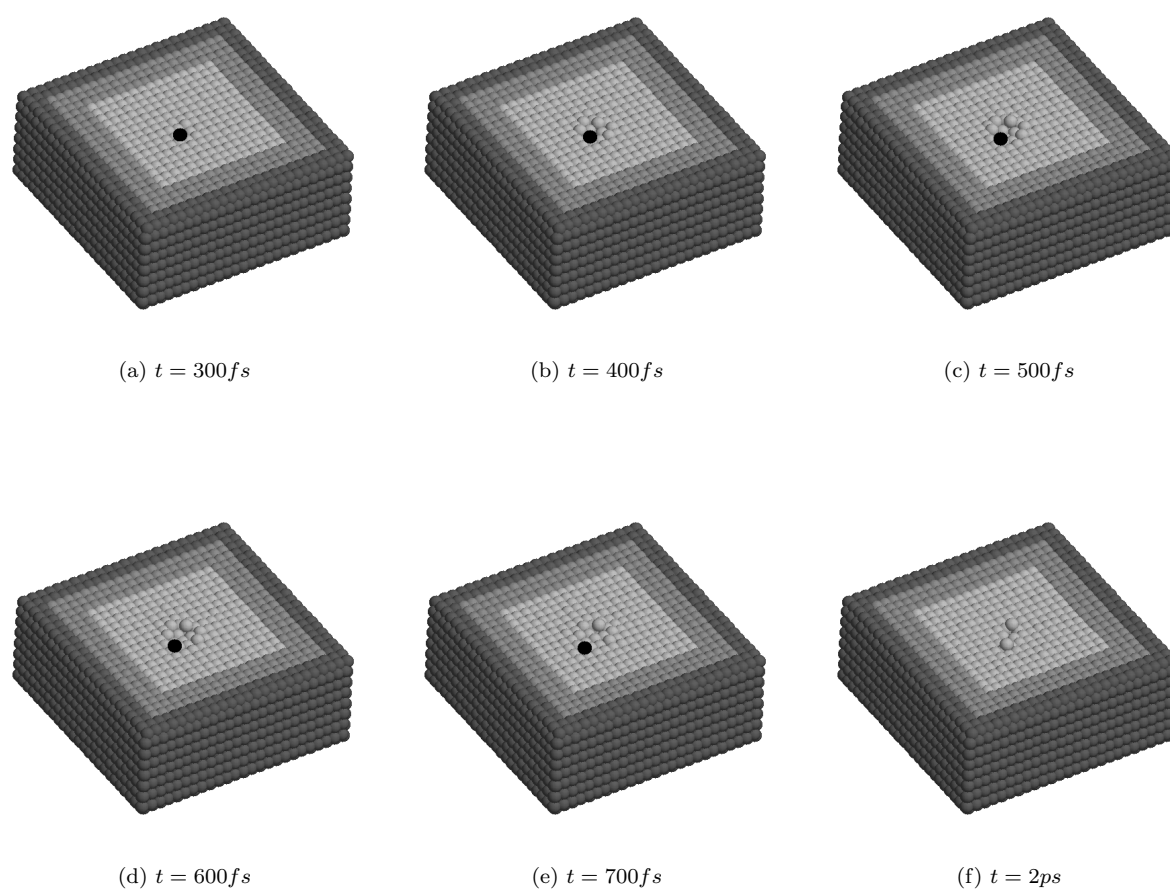


Fig. 6: Snapshots (3D) of a 200 eV Ar^+ -ion normal incidence impact on the $\text{Cu}(001)$ substrate at 1K.

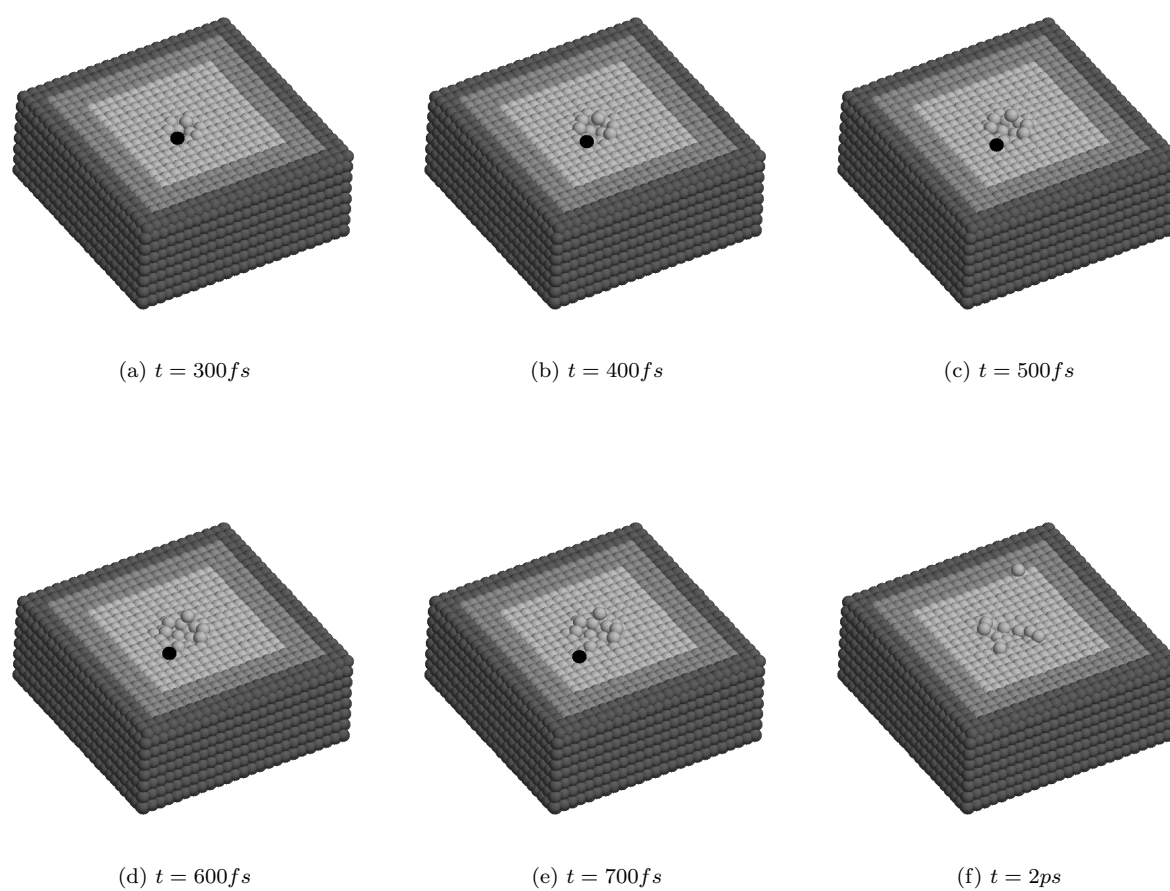


Fig. 7: Snapshots (3D) of a 400 eV Ar^+ -ion normal incidence impact on the $\text{Cu}(001)$ substrate at 1K.